Breathing Mars Air: Stationary and Portable O_2 Generation

Final Report

NIAC Phase I Research Grant #80NSSC22K0763

Ivan Ermanoski, Arizona State University LightWorks® and School of Sustainability
P.O. Box 875402 Tempe, AZ 85287, (480)-727-9644
ivan.ermanoski@asu.edu

Christopher Muhich (Christopher.Muhich@asu.edu), Shuguang Deng (Shuguang.Deng@asu.edu), Ellen B. Stechel (Ellen.Stechel@asu.edu)
Arizona State University

April 2022 – September 2023

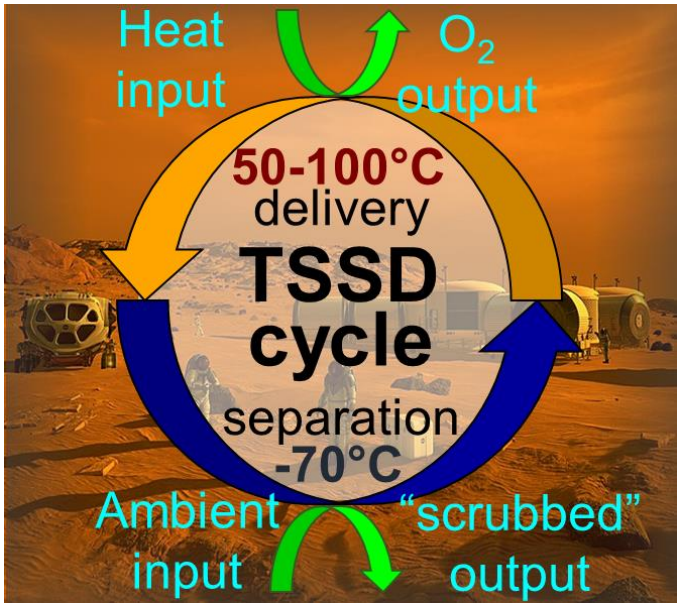

Breathing Mars Air: Stationary and Portable O_2 Generation

Final Report, NIAC Phase I Research Grant #80NSSC22K0763

Prepared by

Ivan Ermanoski, Arizona State University

P.O. Box 875402 Tempe, AZ 85287

EXECUTIVE SUMMARY

PROJECT DESCRIPTION SUMMARY

The main goal of the project was to evaluate the feasibility and utility of a thermally-driven sorption/desorption (TSSD) direct atmospheric harvesting of oxygen for in-situ resource utilization (ISRU) on Mars, using an array of modeling and experimental tools.

The TSSD separation process is a two-step thermally-driven cycle, using a precisely tailored high-surface area oxygen (specifically molecular O_2) sorbent. In the first step, *separation*, O_2 chemisorbs on the sorbent from the atmosphere, near ambient temperature. In the second step, *delivery*, the O_2 desorbs at a target pressure upon heating the sorbent to a desorption temperature. A low ambient temperature facilitates TSSD as it enables oxygen harvesting from partial pressures with low entropy penalties. In effect, TSSD oxygen harvesting leverages natural, solar-driven carbon dioxide splitting, which is responsible the atmospheric oxygen content on Mars.

The project consisted principally of four focus areas: thermodynamic modeling, operational modeling, computational sorbent materials discovery, and sorbent materials synthesis and characterization.

MAJOR FINDINGS

1. The most important finding was the result of thermodynamic and process modeling, showing a broad materials and operating parameter space in which the practical energy input (mostly heat) for oxygen harvesting falls under the theoretical energy input for carbon dioxide splitting (572 kJ/mol_{O2}), and about an order of magnitude below the corresponding practical electrolytical energy input. If realized in practice, TSSD could advance substantially the relevant ISRU state-of-the-art.
2. The number of high surface area sorbent candidates theoretically predicted to have the desirable range of oxygen binding energies is also substantial. One of the experimentally synthesized and evaluated sorbents, a mesoporous yttrium-barium-cobalt oxide, though far from ideal, showed a promising combination of kinetics and oxygen capacity. Sorbent synthesis proved the most challenging aspect of the project.
3. Conceptual TDDS device design, based on existing cooling technology, shows that it is feasible to avoid a packed sorbent (particle) bed design, to minimize the pressure drop (pump

work) in the system, fouling risk from atmospheric dust, device mass, and heat and mechanical energy input.

4. An unexpected finding was that the broadly low energy (primarily heat) input required for oxygen harvesting, when extended to carbon monoxide, includes a substantial materials and operating parameter space in which the energy derived from their reaction is higher than that their harvesting. If realized in practice, this energy return on investment in excess of unity (EROI>1) opens the possibility of using the Mars atmosphere as a net energy source via a "Mars Air Refinery".

RECOMMENDATIONS

The two highest technology risks at this stage, and areas where de-risking is most needed in the course of upcoming technology development steps are both related to sorbent synthesis:

1. Feasibility of synthesizing substituted zeolite sorbents with the desired properties (primarily the oxygen surface binding energy). Of the many sorbent synthesis attempts, the one successful sorbent a was a mesoporous yttrium-barium-cobalt oxide, a high surface area material, but not a zeolite. The particularly appealing aspect of zeolites lies in that all of the atoms in their crystal structure are surface atoms, a fraction of which can be functionalized for oxygen adsorption. Mesoporous materials do not share this property, and the sorption mechanism (depending on particulars) can be combined surface, near-surface, and condensation in pores, lending itself to less well-defined oxygen binding and potentially lower ultimate capacity. Our computational modeling has identified a substantial number candidate substituted zeolites (that are both stable and capable of significant oxygen uptake and release). Substitute zeolites have also been reported in the literature. To de-risk this area and gain confidence in the feasibility of the TSSD process, it is necessary to succeed in synthesizing a handful of the theoretically predicted oxygen-adsorbing substituted zeolites.
2. Synthesizing the desired substituted zeolites serves a second, no less important purpose. Our performance models depend, to some degree, on assumptions regarding the degrees of freedom of adsorbed oxygen molecules. While we have made our best effort to bracket these assumptions based on sound principles, any further model fidelity improvements and refinements would require validation through adsorption/desorption and other suitable experiments performed on target zeolite sorbents.

On the other hand, by far the most potentially far-reaching outcome of the project is the feasibility of using Mars air separation as a net source of energy. For that reason, our third recommendation is:

3. Evaluate in further detail the feasibility of energetically self-sustaining combined oxygen and carbon dioxide co-separation.

ACKGNOWLEDGEMENTS

We gratefully acknowledge the support of the NIAC program and the NIAC team, which has gone above and beyond providing the project funding, and has worked extensively to enable project success through their workshops and conferences, which have resulted in an invaluable amount of highly productive and stimulating discussions.

We are also exceptionally grateful to Dr. Jim Miller (ASU LightWorks®) and our former colleague Dr. Roy Hogan for their indispensable contributions to the project.

We also gratefully acknowledge the extensive use of facilities within the Eyring Materials Center at Arizona State University supported in part by NNCI-ECCS-1542160, as well as the always-helpful Center staff and Dr. Emmanuel Soignard, the senior director of ASU's core facilities operations, at the Eyring Materials Center.

We are grateful to Dr. Michael Hecht, Dr. Donald Rapp, and the entire MOXIE team for making temperature and pressure data at Jezero Crater, the location of the Perseverance Rover and the MOXIE experiment, available for our study, as well as for their constructive and helpful suggestions.

Finally, a significant amount of credit for this project's success is owed to our Ph.D. student Natalia Ali, as well as masters student Zoe Liberman-Martin, and undergraduate students Nicolas Garnand, Jingzhi Xue, Jared Bridges, Ian Padgett, and Iris Calderon

END OF SECTION

Breathing Mars Air: Stationary and Portable O_2 Generation

NIAC Research Grant #80NSSC22K0763

Phase I Final Report

Prepared by

Ivan Ermanoski, Arizona State University

March 2024

1. INTRODUCTION

1.1. BACKGROUND

One of the critical challenges of human Mars missions is the need for *in-situ* resource utilization (ISRU), especially oxygen. In the Reference Architecture,[1] oxygen ISRU is needed as Mars Ascent Vehicle (MAV) or descent/ascent vehicle (DAV) propellant (oxidizer) and for the Environmental Control and Life Support System (ECLSS). A lightweight, reliable, and efficient oxygen supply lowers mission risks and increases the number of achievable objectives per mission.

In addition to the stationary needs of the MAV, ECLSS, and consumables, the Reference Architecture also envisions extravehicular activity (EVA) in small, pressurized "commuter" rovers. At present, the plan is to bring enough oxygen to meet the rover requirements from the habitation area, along with other supplies. Reliable, portable on board oxygen generation could extend rover endurance, broaden the exploration zone from the habitation area, and increase the number of science and resource regions of interest accessible per mission. Furthermore, larger exploration zones ease the tradeoff between landing site appeal (mainly in terms of landing site suitability and associated risk) and proximity to regions of interest.

Efficiency, flexibility, and robustness as the primary features of an effective oxygen generation system. In other words, the system must **(1)** be lightweight and energy-efficient, **(2)** have a flexible operating envelope (e.g., frequent starts/stops and power dips, oxygen-lean source, etc.), and **(3)** be inherently durable and resilient, and minimize potential failure modes and mitigation needs.

The state-of-the-art in the field is the well-known Mars Oxygen ISRU Experiment (MOXIE), which by the end of 2021, produced oxygen over seven experimental runs, under various atmospheric conditions, including day and night, and different seasons.[2] MOXIE is a solid-oxide electrolytic-based approach, which produces oxygen (and carbon monoxide, CO) from carbon dioxide (CO_2) the main component of the Martian atmosphere. MOXIE splits CO_2 at ~800°C, using an electrical input for all functions: compressing and pre-heating the input gas, and for powering the solid-oxide electrolyzer stack.

1.1. MARS OXYGEN HARVESTING: CONCEPT AND INNOVATION

1.1.1. Basic considerations:

While desolate to humans, the Mars atmosphere nonetheless contains molecular oxygen (O_2) albeit at a much lower partial pressure than on Earth, with $pO_{2,amb}$~1 Pa (i.e., ~0.16% out of a total p~636 Pa, most of which is carbon dioxide, CO_2).[3] Notably, the O_2 concentration in the Martian atmosphere is *higher* than that of CO_2 in Earth's atmosphere (0.04%), which is extractable (and in commercialization) via so-called direct air capture (DAC) techniques. Molecular oxygen (O_2) on Mars results primarily from solar photolysis of CO_2:

$$CO_2 + h\nu \rightarrow CO + O \text{ and } 2O \rightarrow O_2. \quad (1).$$

Conceptually, then, oxygen could be sourced directly from the Mars atmosphere. Such sourcing has, though looking at multiple gases, been the subject of a 2000-2001 NIAC Phase I project, the Mars Atmosphere Resource Recovery System (MARRS)[4], which analyzed well-established (though properly targeted) cryogenic gas separation.

The main technical uncertainty of the MARRS process was the technology to compress the thin dusty Martian atmospheric gases efficiently and reliably to the needed processing conditions. Because of the nature of cryogenic separation process, much of the energy input is electricity. Interestingly, one of the recommendations for future study of the MARRS project was the evaluation of adsorption/desorption methods.

Similar thermodynamic considerations motivated our approach, specifically the comparison between oxygen separation and electrolytic CO_2 splitting. The minimum theoretical work to fully separate (strictly, to extract fully) a species from a mixture depends on temperature (T) and the species concentration in the mixture (x) (R is the gas constant) is:

$$W_{min} = -RT\, Ln\left(1/x\right). \quad (2).$$

For O_2 harvesting on Mars, assuming[3] T = 210 K and x = 0.16%, the minimum theoretical extraction work is ~11.2 kJ/mol O_2. This value is only *2% of the enthalpy of CO_2 splitting* (~572 kJ/mol O_2), the current ISRU state-of-the-art.[5]

Put into perspective, a human consumes O_2 at a rate of ~10 mg/s. Ideal extraction could provide this amount using a mere ~3.5 W power input, with small additional power for pressurization.

This large disparity between the minimal energy inputs for extraction and CO_2 splitting gives confidence that even a modestly efficient extraction process (e.g. 5%-10%), even when ancillary needs such as moving and potentially filtering large gas volumes are accounted for, can be far less energy-demanding than even an efficient (e.g., 70%) approach based on CO_2 splitting—assuming such an extraction process can be created.

1.1.2. TSSD Overview

Based on the MARRS and MOXIE experience, an important consideration in devising an oxygen

harvesting approach is the nature of the energy input, specifically thermal vs. electrical. The separation process we evaluated for oxygen harvesting on Mars is *thermal swing sorption/desorption (TSSD)*, illustrated in Figure 1. *TSSD is a two-step thermally-driven cycle*, using a precisely tailored high-surface area oxygen sorbent.

Briefly, in the first step, *separation*, molecular oxygen chemisorbs on the sorbent from the atmosphere, near ambient temperature ($T_{sep} \approx T_{amb}$), removing O_2 from the gas phase to a pressure $pO_{2,sep} < pO_{2,amb}$.[6] In the second step, *delivery*, the O_2 desorbs at a target pressure ($pO_{2,d}$), upon heating to a desorption temperature (T_d). A low T_{amb} facilitates TSSD as it enables harvesting from low pO_2 with low entropy penalties.

In effect, TSSD separation leverages natural, solar-driven CO_2 splitting, which produces the atmospheric O_2 on Mars.

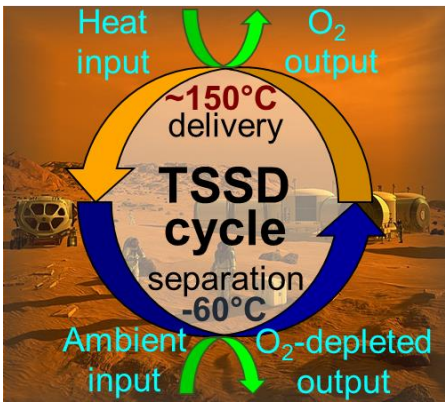

Figure 1. TDDS cycle illustration. In the **separation step** O_2 chemisorbs on the sorbent from the ambient atmosphere at T_{amb} and $pO_{2,sep}$. The **delivery step** releases O_2 at a modest T_d and a target pressure $pO_{2,d}$, eliminating the need for additional pressurization

TSSD is analogous to sorption pumping, which uses molecular physisorption at ~80 K (van der Waals forces), rather than chemisorption (chemical bonds), to bind gases to solids. The two physically different processes also differ in *binding energy* (E_b): typically <10 kJ/mol for physisorption, vs. ≳50 kJ/mol for chemisorption. The stronger, chemisorption-enabled separation driving-force significantly extends the pO_2 and T range for O_2 harvesting, in particular to low pO_2 and temperatures above 80 K (even well above, depending on the binding energy). While use of sorbents has not been typical in harvesting O_2 as a dilute component, sorbents do have a long history as CO_2 scrubbers, including for space flight. By analogy, TSSD might be considered a Mars atmosphere O_2 scrubber.

TSSD is also bears similarities to pressure swing adsorption, another broadly applied sorption-based separation method, and to sorption-based temperature-swing atmospheric water harvesting in desert climates.

An important characteristic of chemisorption is E_b *tunability*. Targeting E_b for O_2 can achieve a significant *reversible oxygen capacity* (high *productivity*), and a desired *selectivity*—achieving primarily O_2 chemisorption, and negligible affinity for other gases. Selectivity against active species, such as CO, CO_2, and H_2O is especially important, but also against the remaining main (inert) atmospheric components, N_2 and Ar. Tunability and selectivity are not possible in physisorption to any meaningful degree.

In the Mars environment, the main component of a TSSD O_2 harvester would be sorbent beds (not necessarily packed beds). The full system must also perform other necessary ancillary functions, such as sorbent heating, heat rejection (and potentially internal solid-solid heat recovery), and inlet/outlet gas handling, with minimal inlet pressurization to minimize electro-mechanical work.

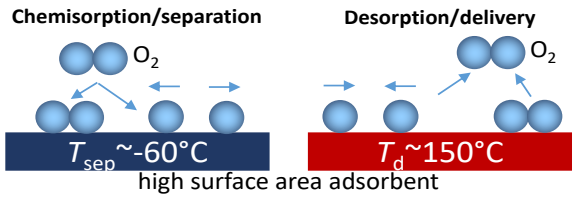

Figure 2. Illustration of the adsorption/desorption processes that are the basis for TSSD.

Broadly speaking then, suitable sorbent candidates would be materials with a high surface area that are also amenable to tuning the binding energy via their composition. These would include zeolites and/or similar materials such as metal-organic frameworks (MOFs), owing to their high surface area and known suitability as general-purpose sorbents. However, known zeolites do not have the necessary O_2 selectivity and capacity, and require compositional modifications (e.g., substitutions) to achieve selective binding. Another class of materials of interest are mesoporous non-stoichiometric metal oxides, i.e. oxides in which the valence of the metal(s) in the crystal lattice can vary, therefore allowing the oxygen content to also vary via the creation and filling of oxygen vacancies in the lattice.[7]

The TSSD concept was in part inspired by our extensive work in oxygen separation in the context of thermochemical cycles, as well as fundamental work in oxygen adsorption/desorption.

1.2. SUMMARY OF PHASE I PROPOSAL TO NIAC AND ADAPTATIONS TO IT

The main goal of the proposed project was to evaluate the feasibility and utility of TSSD for ISRU on Mars, using an array of modeling and experimental tools. This proposed work envisioned a four-pronged approach to extend our computationally identified and experimentally proven high capacity O_2 sorbents for Earth-ambient conditions to the Martian environment and ISRU applications.[7]

The first thrust, gas-solid thermodynamic modeling, serves to understand the space of sorbent properties of interest (especially E_b and T_d), aiming to minimize the energy input per unit O_2 delivered), based on anticipated Mars mission scenarios, locations, needs, and contingencies.

The second thrust was to extend design-point models into a quasi-steady state mass and energy flow models of the system, to simulate "real Mars" performance under the original scenarios, with parameter sensitivity. The main intended outcome of this thrust was preliminary unit sizing (volume and weight).

The goal of the third thrust, computational materials discovery, was to identify candidate materials with E_b values of interest and assess their selectivity against CO_2 and other Martian atmospheric components.

Finally, the fourth thrust focused on synthesizing the most promising sorbent candidates at the lab-scale (1-10 g) and characterizing them using standard material characterization techniques, such as x-ray diffraction, scanning electron microscopy, and thermogravimetric analysis to verify the synthesis and determine the sorption capacity.

In the course of our preliminary work, before project start, and also very early in the project, we discovered that sorbent synthesis is likely to be the highest risk aspect of the project, so we gave it a considerably higher priority than originally intended.

Questions about dust ingress, filtering, and pressure loss in the system and compression work,

and mitigation of these challenges, was another area of increased concern, so we also put added emphasis on the conceptual design of the oxygen separator to de-risk these areas. At the same time, we deprioritized to some extent quasi-steady state modeling and computational materials discovery.

Finally, as a somewhat unexpected positive outcome of the gas-solid thermodynamic modeling thrust, late in the project we extended that work to conceptually include CO capture, with potentially game-changing implications regarding possible approaches to energy supply on Mars.

The above adaptations are evident in the report.

1.3. ORGANIZATION OF THIS REPORT

In Chapter 2 of this Report we describe the methods and results of our gas-solid thermodynamic modeling work. Historically, this was the earliest part of the work preceding the project and most relevant for the conceptual feasibility of TSSD oxygen harvesting on Mars (and oxygen separation in general).

Chapter 3 describes the experimental methods and results regarding sorbent synthesis and characterization, showing both the challenges in synthesizing target sorbents, but also the considerable leap in sorbent performance, in particular kinetics, that derives from the highly porous structure.

Chapter 4 describes our work in computational sorbent screening. Although conceptually computational screening precedes synthesis, we opted to present synthesis first, as it transpired as one of the most challenging parts of the project on the success of which the concept rests.

Chapter 5 describes the considerations and outcomes of our TSSD device conceptual design and shows that approaches inspired by direct air capture of CO_2 on earth can be adapted for oxygen harvesting on Mars.

Chapter 6 briefly discusses unexpected but potentially very consequential results, regarding the feasibility of creating self-sustaining separation, by leveraging the presence of CO in the Mars atmosphere.

Chapter 7 briefly summarizes our education and outreach efforts during the project, and Chapter 8 summarizes directions for potential relevant future studies.

1.4. RELATED TECHNOLOGY

As mentioned earlier in this chapter, the two main technologies related to oxygen generation on Mars are cryogenic separation (MARRS) and carbon dioxide electrolysis (MOXIE).

2. GAS-SOLID THERMODYNAMIC MODELING

2.1. MODELING APPROACH AND BASELINE ASSUMPTIONS

A simple model captures the essential thermodynamics of the process, based on a regular solution model for the 2D gas of adsorbed oxygen. Microscopically, the processes of interest are *dissociative chemisorption*, where O_2 dissociates on adsorption, and each occupied adsorption site binds an individual oxygen atom and molecular chemisorption, where each occupied adsorption site binds an oxygen molecule. The occupied fraction of the available adsorption sites is typically known as *coverage* (θ), a dimensionless quantity with values between 0 and 1. Labelling the clean sorbent as Σ, and the adsorbed system O/Σ, the combined system Gibbs free energy (normalized per sorbent atom) is:

$$G_{\mathrm{O}/\Sigma}(\theta,T) = (1-\lambda\theta)G^0_{\Sigma}(T) + \lambda\theta G^0_{\mathrm{O}/\Sigma}(T) + \lambda\Delta G_{mix}(\theta,T) \quad (3).$$

Here λ is the number of adsorbate sites per sorbent atom (including bulk atoms, i.e. those not available to the adsorption/desorption process). For simplicity and purposes here, ΔG_{mix} includes only ideal configurational entropy, i.e., $\Delta G_{mix}(\theta,T) = -TS_{conf}(\theta)$, where:

$$S_{conf}(\theta) = -R(\theta ln\theta + (1-\theta)ln(1-\theta)) \quad (4),$$

and R is the universal gas constant. There is sufficient precedent that sub-lattice models can accurately describe phase behavior in several systems.(Olson and Kuehmann, 2014)[8].

In such a model, there are three terms: (1) binding energy, (2) sensible enthalpy and entropy of the material (both derived from the heat capacity), and (3) mixing entropy. We employ the Einstein model, with a single Einstein temperature (T_E) independent of coverage to represent both the clean (Σ), and O-covered sorbent (O/Σ) and to capture the free energy from vibrational modes. The sublattice model represents the Gibbs free energy and is used to determine equilibrium adsorbate coverage as a function of temperature and p_{O2} in the gas phase. At equilibrium, the oxygen chemical potential in the condensed phase must equal the chemical potential in the gas phase. The latter depends on temperature and on p_{O2}. The former depends on temperature and coverage. Thus, in the separation step, at T_{amb} and $p_{O2,amb}$ the system equilibrates and a coverage θ_{amb}. In the delivery step (sorbent regeneration or activation), at T_{act} and $p_{O2,deliver}$, the system equilibrates at θ_{act}.

To derive the equations for θ_{amb} and θ_{act}, note that at equilibrium $\delta G = 0$, for an infinitesimal change in θ, adding (or subtracting) an oxygen atom to the adsorbate system and subtracting (or adding) one oxygen atom to the gas phase i.e., the reaction:

$$\frac{1}{d\theta}\mathrm{O}/\Sigma(\theta) \leftrightarrow \frac{1}{d\theta}\mathrm{O}/\Sigma(\theta+d\theta) - \tfrac{1}{2}O_{2,gas} \quad (5),$$

$$\frac{1}{d\theta}G_{\mathrm{O}/\Sigma}(T,\theta) = \frac{1}{d\theta}G_{\mathrm{O}/\Sigma}(T,\theta+d\theta) - \tfrac{1}{2}G_{O_{2,gas}}(T,p_{O2}) \quad (6).$$

Rearranging and taking the limit $d\theta \rightarrow 0$, yields the fundamental equation that defines the

equilibrium condition at θ:

$$\frac{dG_{O/\Sigma}(T,\theta)}{d\theta} = ½G_{O_{2,gas}}(T, p_{O2}) \quad (7).$$

The right-hand-side (gas phase) is well-known and can be obtained from a number of sources, such as NIST Chem Webbook or HSC,(*HSC Chemistry 9*, n.d.; *NIST Chemistry WebBook, NIST Standard Reference Database Number 69, Eds. P.J. Linstrom and W.G. Mallard*, n.d.) and is the chemical potential of O in the gas phase. The left hand side is the chemical potential of adsorbed O on the surface of the sorbent. Multiplying Equation 7 by $\beta = 1/RT$ renders the equilibrium condition unitless. Let then $\tilde{\mu} = -\beta G = S/R - \beta H$ be a unitless state potential, noting that $G = H - TS$, where S and H are the entropy and enthalpy, respectively. Substituting the unitless $\tilde{\mu}$ into the above equations, and changing variables, produces the unitless equilibrium relationship between the sorbent (on the left-hand side) and the gas phase (on the right-hand side):

$$\frac{d\tilde{\mu}_{O/\Sigma}(\beta,\theta)}{d\theta} = ½\tilde{\mu}_{O_2}(\beta, p_{O2}) = ½\tilde{\mu}_{O_2}(\beta; p_{O2} = p_{ref}) + ½ln(p_{ref}/p_{O2}) \quad (8).$$

Hence, the equilibrium conditions for pumping (adsorption) and activation (desorption) are:

$$\frac{d\tilde{\mu}_{O/\Sigma}(T,\theta_{amb})}{d\theta} = ½\tilde{\mu}_{O_{2,gas}}(T_{amb}, p_{O2,amb}) \quad (9),$$

$$\frac{d\tilde{\mu}_{O/\Sigma}(T,\theta_{act})}{d\theta} = ½\tilde{\mu}_{O_{2,gas}}(T_{act}, p_{O2,deliver}) \quad (10).$$

Combining the three terms, namely binding energy, sensible (enthalpy and entropy using an Einstein model), and the ideal entropy of mixing, yields:

$$\tilde{\mu}_{O/\Sigma} = \beta\lambda\theta E_b + 3(1+\lambda\theta)\left(\tilde{\mu}_E\left(\frac{T_E}{T}\right) + 3\frac{{}^{T}/_{T_E}}{e^{T_E/T_0-1}}\right) - \lambda(\theta\cdot\ln\,\theta + (1-\theta)\cdot\ln(1-\theta) \quad (11),$$

where:

$$\tilde{\mu}_E(x) = x - \ln(e^x - 1) \quad (12).$$

All the results below stem from setting the oxygen potential on the sorbent equal to the oxygen potential in the gas phase for the two conditions, temperature and p_{O2}, for pumping and then for activation with a single fixed T_E = 217 K.

The sensible heat requirement for heating the adsorbate/solid system follows from its specific heat capacity, based on the above Einstein model, with the simplification that T_E is the same for the sorbent bulk, bare surface, and oxygen-covered surface. The value of λ (in Equation 3) is necessary for this calculation, but is not known *a priori*, and depends on two factors, of which one is the specific surface area of the solid. The typical surface area measure, area per unit mass (e.g.

$m^2\ g^{-1}$) is not directly relevant for this application. Rather, it is the ratio of surface atoms to the total number of atoms in the solid: *surface atom fraction*, ν_s.

To gauge the range of feasible ν_s values, some common low-cost examples of high-surface area materials, such as zeolites and activated carbon, are helpful. The structure of many penta-sil-zeolites (e.g. ZSM-5) is well understood. Nearly all ZSM-5 atoms can be considered surface atoms, as they form the walls of nanoscale channels that give the materials their high characteristic (internal) surface area. For activated carbon, a highly disordered form of graphite, the surface atom fraction can be estimated based on the per-atom surface area of a graphite unit cell in an infinite 2D sheet. Accounting for both sides of the hexagonal cell surface, this area can be shown to be $5.24 \cdot 10^{-20}$ m^2, corresponding to ~31550 $m^2\ mol^{-1}$ or ~2630 $m^2\ g^{-1}$. Considering that gas adsorption measurements show values of ~3000 $m^2\ g^{-1}$, all atoms in activated carbon can be considered surface atoms. These examples give confidence that materials processing methods can be used to create high-surface area oxygen sorbents, or that existing high-surface area materials can act as adequate supports.

The second component of λ is the theoretical surface coverage (ν_{max}), determined by the number of adsorption sites per surface atom, i.e. the fact that not all surface atoms are necessarily adsorption sites. Therefore, $\lambda = \nu_s \cdot \nu_{max}$.

The required pumping heat input (per mole O, Q_{mol}) also depends on the *reversible coverage*: $\Delta\theta = \theta_{amb} - \theta_{act}$. The relationship between θ on one hand, and T_{act}, T_{amb}, and E_b follows from the adsorption desorption model, described above. In broad terms, reaching near-unity coverage on adsorption requires a low T_{amb} and high E_b, whereas reaching a near-zero coverage on activation requires a high T_{act} and low E_b.

In summary, Q_{mol}, a sum of the binding energy and sensible heat (Q_{sens}) can be expressed as:

$$Q_{mol} = E_b + Q_{sens} = \frac{H(T_{act},\theta_{act}) - H(T_{amb},\theta_{amb})}{\theta_{amb} - \theta_{act}} (1-\varepsilon) + \frac{1}{2} H_{O2}(T_{act}) + \varepsilon E_b \qquad (13),$$

where ε is the sorbent solid-solid heat recovery effectiveness. The sorbent captures O_2 at $p_{O2,amb}$, and is activated by desorption into the delivery atmosphere ($p_{O2,act}$).

The difference between the dissociative and molecular chemisorption is numerical (i.e. one molecule, not atom, per filled site), and with respect to the remaining degrees of freedom in the enthalpy calculation. For example, in the gas phase an oxygen molecule has two rotational degrees of freedom, and on the surface it has one. An oxygen atom on the surface, however, has no rotational degrees of freedom. Similar distinctions must be made with respect to vibrational degrees of freedom.

Baseline model assumptions also include a relatively low density of adsorption sites: λ = 1/60 (achieved, for example, by setting ν_s = 1/2 and ν_{max} = 1/30, i.e., surface atoms are half of the total atoms, and there being one adsorption site per thirty surface atoms or per six unit formulas of

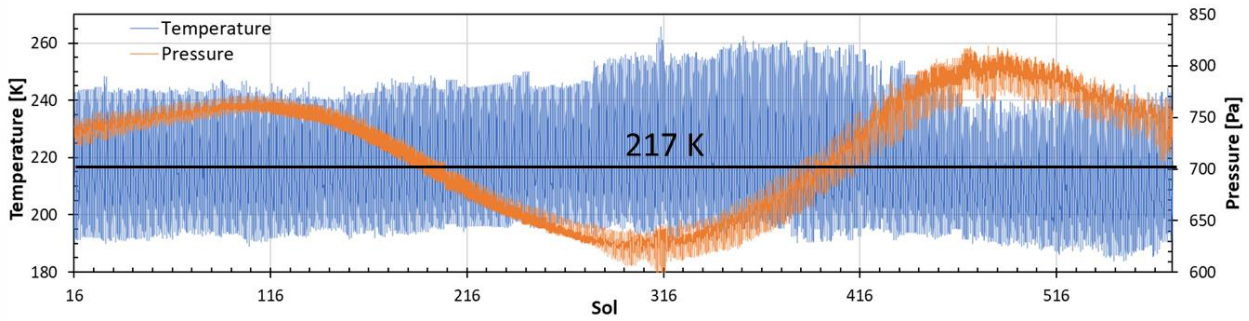

Figure 3. Temperature and pressure at Jezero Crater, the location of the Perseverance Rover and MOXIE experiment. 217 K is the average temperature for the data period. We are grateful to Dr. Michael Hecht, Dr. Donald Rapp, and the entire MOXIE team for making this data available for our study.

an ABO_3-type oxide or per five unit formulas of an $AlPO_4$ type zeolite). The assumption is largely guided by understanding of the limit of zeolite structures and their capacity for substitution, which is a field in development. The baseline solid-solid heat recovery effectiveness is $\varepsilon = 0.5$.

The baseline ambient temperature T_{amb} = 217 K, based on data from the Perseverance Rover (Figure 3), and the baseline delivery pressure is 20 kPa.

2.2. RESULTS

The intermediate resulting outputs of these models are *reversible oxygen coverages* $\Delta\theta = \theta_{sep} - \theta_d$ (directly related, but not identical to the reversible oxygen capacity)

The reversible coverages $\Delta\theta(E_b)$ the baseline case and several T_{act} are shown in Figure 4. The results shows that $\Delta\theta$ is negligible (or negative) at low E_b, and then increases with increasing E_b. Maxima occur with further E_b increase, and $\Delta\theta$ then decreases again to negligible values. Recalling that $\Delta\theta = \theta_{amb} - \theta_{act}$, this behavior can be understood in terms of the dominant coverage in the process. At low E_b, θ_{amb} is low, reflecting the inability of the substrate to bind much oxygen. The cycle for low E_b, then, is between two low coverages. At high E_b, θ_{act} is also high, reflecting the strong binding that prevents oxygen desorption at T_{act}, creating a cycle between two high coverages. Reversible coverage maxima occur where the two coverages are optimally balanced.

Values for the binding energy that give the highest $\Delta\theta$ (E_b ~55-70 kJ/mol$_{O2}$) fall near the low end of the range for chemisorption, indicating mild requirements for a separation process. Such E_b values for oxygen chemisorption can, for example, be found on the surfaces of precious metals. Note that, in principle, unique values of E_b in Figure 4, each correspond to different sorbents, reflecting an inverse materials design challenge.

The low reversible coverage for

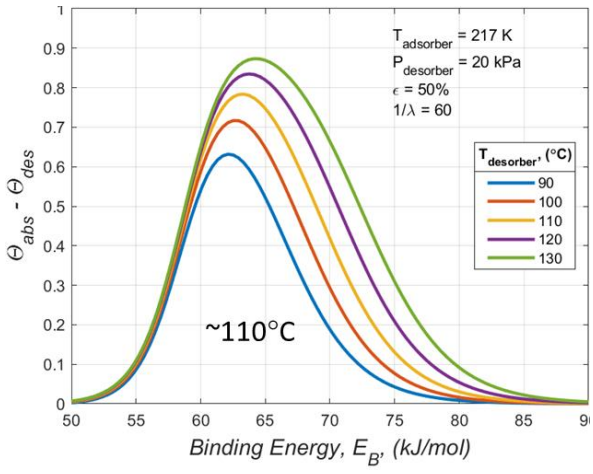

Figure 4. Reversible oxygen coverage $\Delta\theta$ for the baseline case.

E_b <~50 kJ/mol$_{O2}$ (~0.36 eV per atom) also illustrates the need for chemisorption as the adsorption mechanism. With E_b in the typical physisorption range (~1-10 kJ/mol), the reversible coverage (for adsorption at 217 K) would be negligible.

From the coverage characteristic follows *separation heat requirements* (Q_{mol}), typically expressed per mole O_2, such as shown in Figure 5. The values of Q_{mol} for all temperatures exhibit minima (Q_{min}) near, albeit not coinciding, with $\Delta\theta$ maxima.

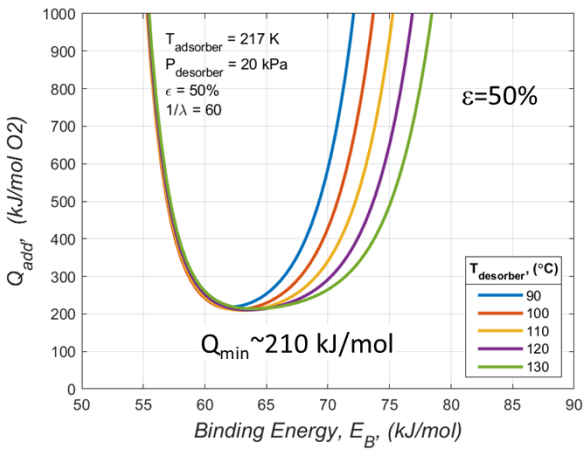

Figure 5. Separation heat input.

The most important outcome of the baseline calculation is that the required heat input for oxygen separation Q_{min}~210 kJ/mol$_{O2}$ is substantially lower than even the theoretical enthalpy of CO_2 splitting (572 kJ/mol$_{O2}$). For reference, assuming one person consumes 1 kg of oxygen per day, the broad 210 kJ/mol$_{O2}$ minimum corresponds to a heat rate of $\dot{Q}$~75 W/person.

Before going further into the details of various scenarios, it bears re-emphasizing that TSSD input need not be electrical, as the process is by its nature thermally driven. This distinction is of significant importance in the Reference Architecture, where the preferred power source is nuclear (owing to much lower launch mass than solar PV, for example, and the long periods of poor sunlight during dust storms). In this architecture, TSSD can circumvent much of the poor efficiency (and therefore added generator mass) from the ~6% heat-to-electricity conversion.

One example where the low heat rate comes into contrast is in pressurized "commuter" rovers (anticipated crew of two, 100 km and 1 week endurance), O_2 from TSSD would require far less power (150 W) than rover mobility (25 kW$_e$) and could significantly extend endurance and the number of science and resource regions of interest accessible per EVA and per overall mission.

Turning to relevant sensitivities, we analyzed two limiting cases. The first is a low temperature case, exploring the limits of how well TSSD can operate if confined to the lowest ambient temperatures, an advantage for an adsorption process, but a disadvantage from a capacity factor standpoint. The other motivating factor for probing the low temperature limit stems from the understanding that Jezero Crater is at a somewhat “balmy” location near the Mars equator (18°N) and elevation approximately minus 2600 m below the Mars Areoid. Mid-latitude and mid-elevation locations are certain to be colder.

We also examine limiting cases of solid-solid heat recovery. The lower value, ε = 25%, is likely to not represent a challenge in device design and also shows the effect on performance that might be expected if solid-solid heat recovery is not included at all. The higher value, ε = 75%, serves to probe the upper performance range, understanding that high heat recovery often incurs a kinetics or a mass penalty or both, and that these must always be part of the consideration

in detailed system design and optimization.

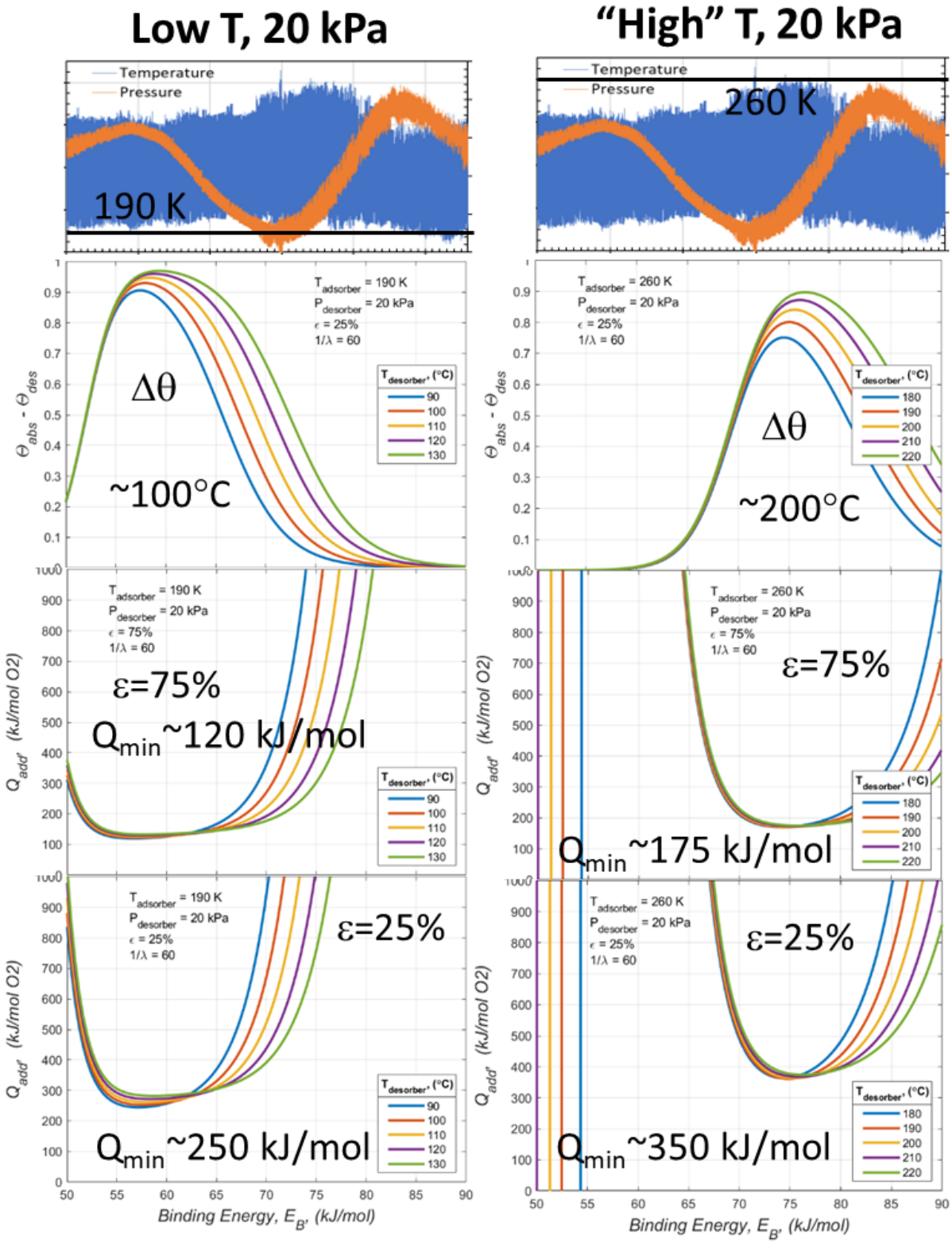

Figure 6. Separation heat input for two limiting cases and two solid-solid heat recovery values each.

As expected, Q_{min} for the low temperature case (T_{amb} = 190 K) is lower than the baseline, however not so lower that it might justify oversizing the system (capture and storage) to take advantage of favorable operating conditions at Jezero-like locations. Another result of interest is the effect of ε on the shape of the Q curves: At high ε the minima are broader, indicating a secondary value of high solid-solid heat recovery, namely that the binding energy needn't be precisely tuned. The value stems from the fact that different adsorption sites, somewhat but not too different (which is not unusual in real sorbents), may participate in the separation process.

At the "high" temperature limit (T_{amb} = 260 K) the overall behavior of the results is also as expected, namely the overall Q_{min} increase compared to the baseline case. Of note is also the activation temperature increase to ~200°C. Note also the computational artifacts generated at the transition between positive negative $\Delta\theta$ at low binding energies. These could be artificially removed, but we show them for illustration purposes.

While many other cases could be considered, we present here one more that could be of unexpected interest, namely when the delivery pressure is 1 kPa, i.e. not much above the local ambient pressure. The ambient temperature is the same as the baseline: T_{amb} = 217 K. This case was initially motivated by the desire to probe the pressure sensitivity of the required heat input, but also by the potential value of storing oxygen in relatively lightweight inflatable envelopes (bladders) with minimal hoop stress requirements and therefore also minimal weight. The latter would be useful in use cases that do not by their nature require oxygen to be pressurized, such as catalytic recombination of fuels (however produced) with oxygen, for heat generation.

Again, the result is qualitatively expected, but is quantitatively interesting as it is a mere 20% of the enthalpy of CO_2 splitting and could decrease further at lower T_{amb}.

At this point we again note that different binding energies conceptually correspond to different sorbents, meaning that in the final design the choice of sorbent will substantially depend on the anticipated operating scenario and overall optimization objectives, which could differ for stationary life support, rovers, for propellant, or for re-use in a catalytic oxidation process.

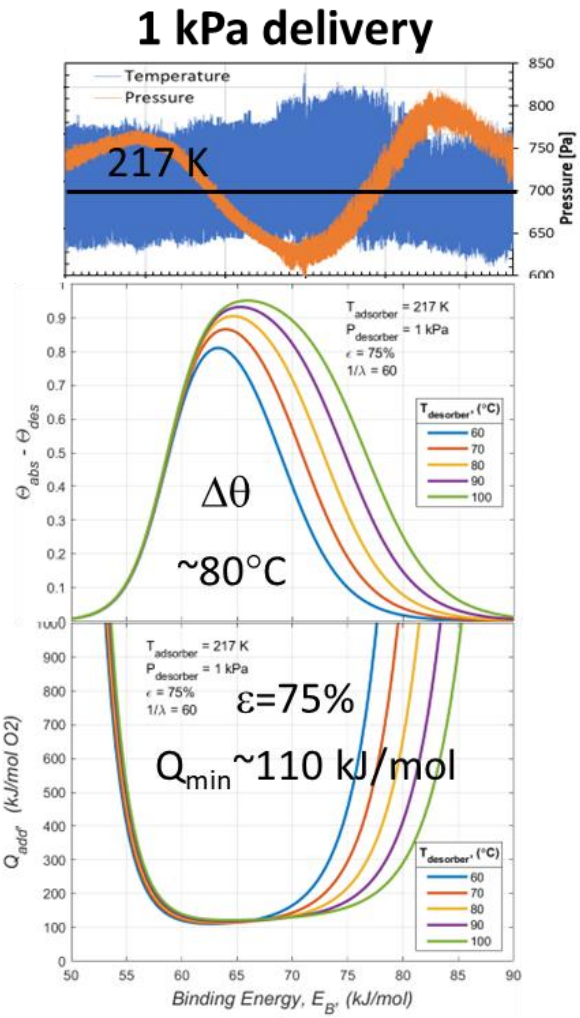

Figure 7. Separation heat input for average ambient temperature operation and near-ambient pressure oxygen delivery .

The distinction between electrical and thermal input bears re-emphasizing, here. A nuclear power plant heat rate $\dot{Q}$ = 1 kW_t produces P = 60 W_e of power, i.e. 1 kW_t⇔60 W_e. We will also recall here that TSSD can be tuned to deliver O_2 at a target pressure (with additional heat input), eliminating the need for additional mechanical compression work and thermal→electrical→mechanical conversion.

The most important outcome of the gas-solid thermodynamic modeling is that a substantial parameter and operating space exists in which heat input for oxygen harvesting is substantially lower than even the theoretical enthalpy of CO_2 splitting, and especially the practical primary thermal input for electrolytic CO_2 splitting using radio thermal generator (RTG) heat-to-electricity conversion.

3. SORBENT SYNTHESIS AND CHARACTERIZATION

Experimental sorbent research for the project focused on two classes of materials: substituted zeolites and porous non-stoichiometric metal oxides, illustrated in Figure 8.

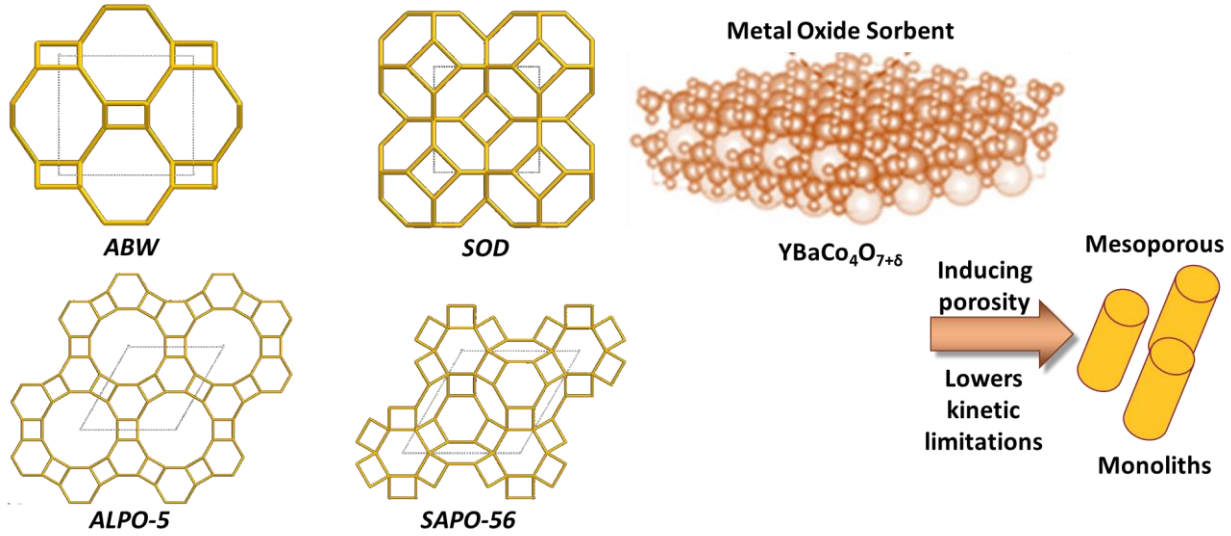

Figure 8. Examples of the two sorbent materials. The first four are zeolite frameworks, and the latter is a non-stoichiometric metal oxide. While the two classes have fundamentally different sorption mechanisms, at large specific surface areas some of these mechanisms start to converge.

3.1. ZEOLITE SYNTHESIS AND CHARACTERIZATION

Throughout course of this project, following computational screening results detailed in Chapter 4, we made 47 zeolite synthesis attempts, including seven different zeolite frameworks, and developed two different zeolite synthesis methods, in addition to following published methods.

We refer to the zeolite samples both by the material name abbreviation (i.e. AlPO-5 for aluminophosphate-five) and their three-letter framework code assigned by the International Zeolite Association (IZA). The first substituted zeolite framework we attempted was Aluminophosphate-five (AFI/AlPO-5). Figure 9 shows a generalized method for synthesizing aluminophosphate zeolites. We developed a hydrothermal synthesis method based on published results for Fe-substituted AlPO-5 samples.[9]

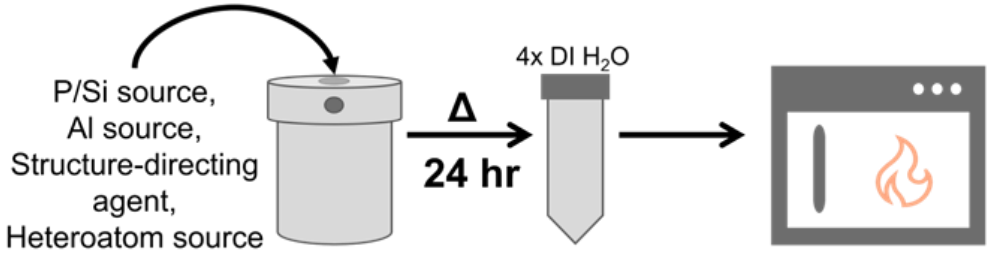

Figure 9. Generalized hydrothermal synthesis for AlPO zeolites, depicting crystallization, washing, and calcination.

In the method we developed, an AlPO-5 crystallization solution was prepared with the molar

ratios:1Al_2O_3:1.3P_2O_5:1.6TEA:xM:100H_2O, where M is a metal heteroatom of interest, identified by theoretical predictions. For our initial syntheses, we focused on xM:1 Al molar ratios where x = 0.05, 0.075, 0.1, and 0.15. M was primarily Ce or Mo ions from cerium nitrate hexahydrate and ammonium molybdate, respectively. We made the solution by combining an aluminum source (aluminum isopropoxide), a phosphorous source (phosphoric acid, a heteroatom source, an organic structure-directing agent (triethylamine), and deionized water while stirring under ambient conditions in a glass beaker. First, we combined stoichiometric amounts of aluminum isopropoxide and deionized water. After stirring for three hours on a magnetic stir plate, we added the remaining precursors dropwise, after dissolving the solids in a small volume of deionized water. We stirred the solution for one hour after the addition of each chemical precursor, then stirred for 24 hours under ambient conditions. The total solution volume amounted to one-third of the total autoclave volume (~ 50 mL). After mixing, we heated the synthesis solution in a 150 mL Parr autoclave reactor with a PTFE liner at 180 ˚C for 24 hours. After crystallization, we then cooled the reactor at ambient conditions overnight. We washed the zeolite crystals repeatedly via centrifugation (1000 RPM for 10 min) utilizing fresh deionized water after each round of washing, until a neutral pH was achieved. After washing, we dried the zeolites at ambient pressure overnight at 120 ˚C, then calcined the sample for eight hours at 650 °C to burn off the organic structure directing agent.

We characterized the zeolite samples with powder X-ray diffraction (XRD) to obtain crystallographic structure data, using a Malvern PANalytical Aeris diffractometer from the Eyring Materials Center at ASU (supported in part by NNCI-ECCS-1542160). Our AlPO-5 synthesis method was validated by the observation of characteristic peaks for AlPO-5 at 2ϑ = 7.5˚ and 2ϑ = 19-22˚ (Figure 10). We completed oxygen adsorption experiments at 25 °C and 1 bar on a Micromeritics 3 Flex adsorption apparatus after degassing the samples for 24 hours at 400 °C. After evaluating Mo-substituted and Ce-substituted samples on the 3flex, we realized that we were not observing oxygen adsorption capacities that correspond to chemisorption at room temperature. This led us to look for other characterization methods to help us understand our synthesized samples and the degree of framework substitution in them.

We attempted to characterize our 0.1 Mo AlPO-5 sample with atomic adsorption spectroscopy (AAS). However, AAS showed no Mo ion signal in the adsorption spectra. This result, combined with the lack of oxygen adsorption from the 3 flex experiments indicated that our zeolite samples did not have heteroatom substitution.

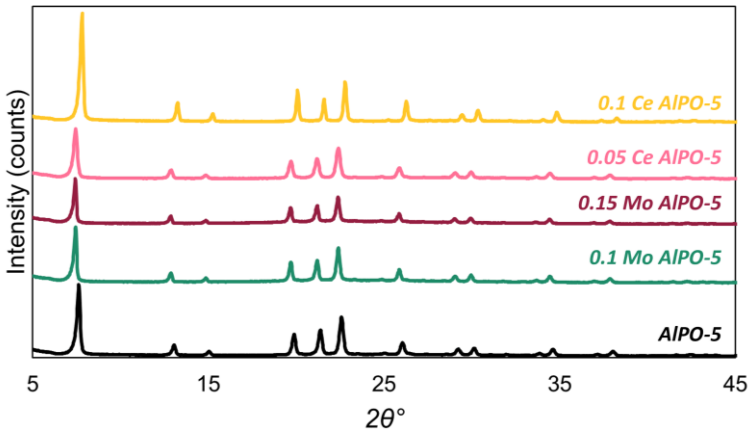

Figure 10. XRD pattern of 0.1 Ce AlPO-5 (yellow line), 0.05 Ce AlPO-5 (pink line), 0.15 Mo AlPO-5 (maroon line), 0.1 Mo AlPO-5 (green line) and unsubstituted AlPO-5 (black line).

To overcome this challenge,

we revised our synthesis approach to promote substitution into the zeolite framework. We developed the "Al-last method" in which the metal heteroatom precursor was added to the synthesis mixture before the aluminum isopropoxide solution. First, we dissolved the heteroatom metal sources in water and added the solution dropwise while stirring into a phosphoric acid and water mixture. Then, we added the structure directing agent dropwise. We stirred the mixture for an additional hour before adding the aluminum source. Theoretically, this would allow the heteroatom and phosphorus ions to bond with the structure-directing agent, before introducing the preferred 3^+ aluminum source.

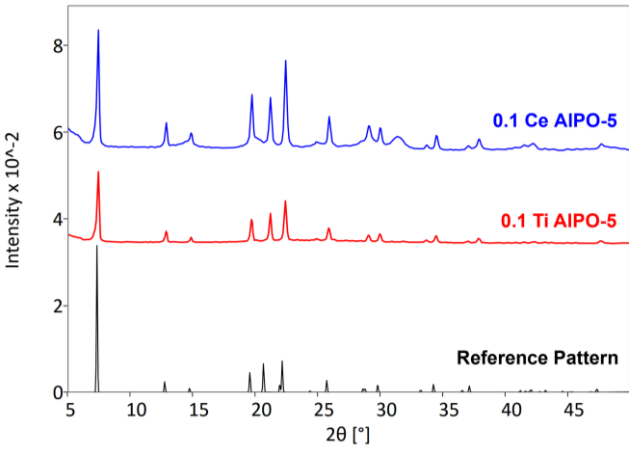

Figure 11. XRD pattern of 0.1 Ce AlPO-5 (blue line) and 0.1 Ti AlPO-5 synthesized using the Al-Last method. AlPO-5 reference pattern (black line) is provided by IZA.

We validated the Al-last synthesis method by characterizing the synthesized samples with XRD. The observation of characteristic peaks for AlPO-5 at 2ϑ = 7.5˚ and 2ϑ = 19-22˚ (Figure 11) indicates that changing the addition order of Al and P does not disturb AlPO-5 crystallization. However, when we evaluated our Al-last AlPO-5 samples on the 3flex, we still did not observe oxygen adsorption capacities that could correspond to chemisorption. We then characterized one of our Al-last 0.1 Ce AlPO-5 samples with scanning electron microscopy (SEM) (Figure 12). We confirmed the presence of cerium atoms in the new AlPO-5 sample with energy-dispersive X-ray spectroscopy (EDS). The EDS spectra showed that the new Ce/AlPO-5 sample contained 2% cerium and had a 0.286 Ce/Al ratio, suggesting that less aluminum was incorporated into the zeolite structure.

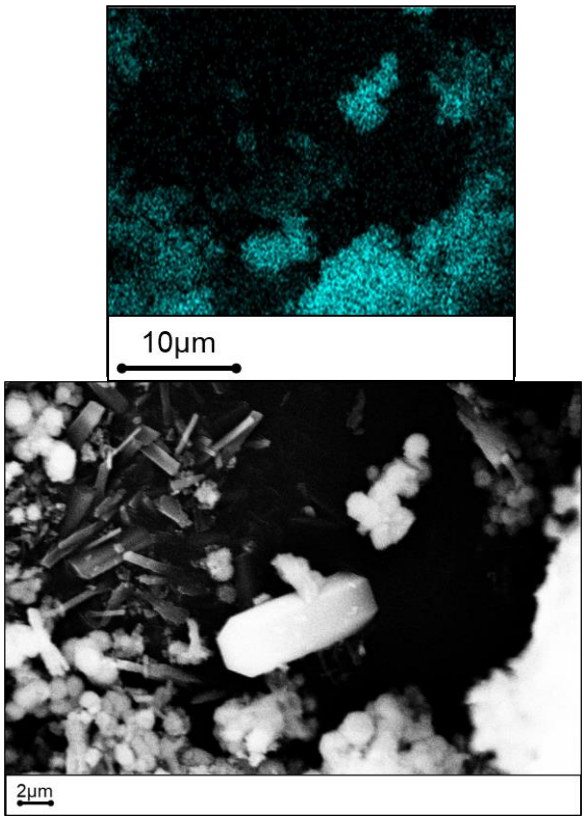

Figure 12. EDS image of 0.1 Ce AlPO-5 synthesized with the Al-Last method (Top) and the SEM image it is based on (Bottom).

While the EDS confirmed that there were Ce atoms in the AlPO-5 sample, the lack of oxygen adsorption during 3Flex experiments suggested the 0.1 Ce AlPO-5 sample did not have Ce atoms substituted into the zeolite framework. We hypothesized that the Ce atoms in this sample were sitting on the surface of the crystals or in the pores, instead of replacing framework Al atoms. These

conclusions led us to look toward other zeolite frameworks that had been theoretically predicated to chemisorb oxygen when substituted with the metals that we had available (mainly Ce, Mo, Sn, Ti, and V).

Using the Al-Last method, we then branched out from the AlPO-5 framework to investigate other zeolite frameworks that would yield the correct oxygen binding energy when substituted with heteroatoms of interest. We decided to start with other aluminophosphates, as those frameworks are most similar to ALPO-5 both in structure and synthesis method. We used the Al-last method to synthesize all other zeolite frameworks, using the crystallization times and temperatures listed in the International Zeolite Association's (IZA) book of verified synthesis methods.[10]

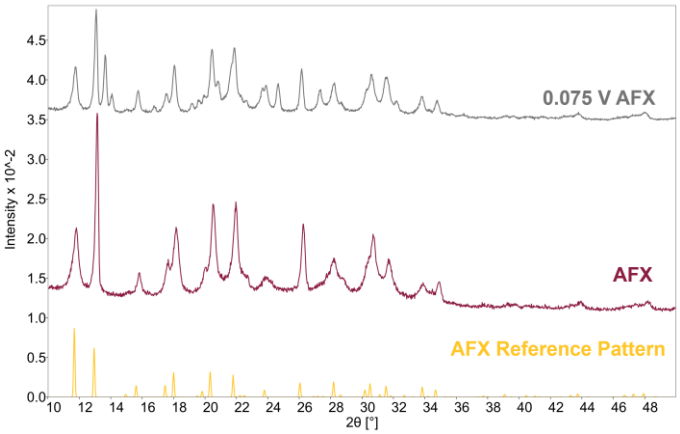

Figure 13: XRD pattern of 0.075 V AFX (gray line) and unsubstituted AFX (maroon line) synthesized using the Al-Last method. Calculated AFX reference pattern (yellow line) is provided by IZA.

We first synthesized VPI-5 with the same method as ALPO-5, using dipropylamine (DPA) as the structure-directing agent, instead of triethylamine. We prepared our VPI-5 crystallization solution with the molar ratios: $1DPA:1P_2O_5:1\text{-}xAl_2O_3:40H_2O$. We encountered challenges while synthesizing VPI-5, after calcination the VPI-5 structure was not stable.

When we observed VPI-5 structures with XRD, we noted a large amorphous phase. We then moved on to SAPO frameworks (SAPO-11/AEL and SAPO-56/AFX), which are like AlPO frameworks, but have different framework geometries because some of the framework P ions are substituted with Si. We hypothesized that this substitution of Si would facilitate framework substitution of other heteroatoms. We synthesized AFX crystals in a similar manner to AlPO-5, using the Al-last method with N,N,N',N'-Tetramethyl-1,6-hexanediamine (TMHD) as the structure directing agent and tetraethyl orthosilicate as the Si source. We prepared our AFX crystallization solution with the molar ratios: $2TMHD:xM:1P_2O_5:0.8\text{-}xAl_2O_3:0.6SiO_2:40H_2O$. We verified the Al-last synthesis method for AFX with XRD (Figure 13). Later, we also worked with the AEL/SAPO-11 framework, using DPA as the structure-directing agent. We prepared our AEL crystallization solution with the

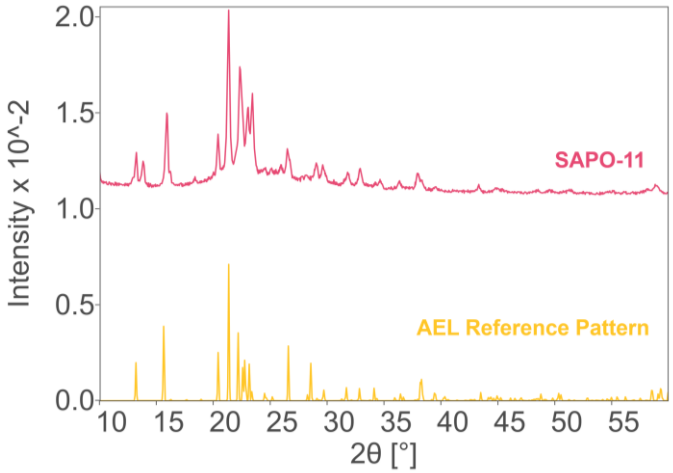

Figure 14. XRD pattern of AEL/SAPO-11 (pink line) synthesized using the Al-Last method. Calculated AEL reference pattern (yellow line) is provided by IZA.

molar ratios: 1DPA:xM:0.2SiO_2:1P_2O_5:1-xAl_2O_3:20H_2O. We also verified the Al-last synthesis method for AEL/SAPO-11 with XRD (Figure 14).

After working with the AlPO and SAPO frameworks, we also considered three aluminosilicate frameworks, ABW, SOD and LTA. We synthesized all aluminosilicate frameworks with the Al-last method, making revisions as necessary to accommodate aluminosilicate crystallization conditions. The changes we made to the synthesis methods were as follows: we exchanged aluminum isopropoxide with sodium aluminate for the Al source, added fumed silica as the Si source, added lithium chloride or sodium bromide as cation sources, and used sodium hydroxide to make the synthesis solutions basic (pH=11-13). We first synthesized ABW the molar ratios: 1Li_2O:0.5-xAl_2O_3:1SiO_2:xM:100H_2O. We synthesized SOD crystals in a similar manner to ABW. We prepared our SOD crystallization solution with the molar ratios: 0.9-x$AlOH_3$:1SiO_2:12.5NaOH:7.5NaBr:xM:144H_2O. We verified the synthesis of both unsubstituted SOD and 0.1 Ti SOD with XRD (Figure 15). The last aluminosilicate we synthesized with the Al-last method was LTA. Our LTA crystallization solution was prepared with the molar ratios: 3.165Na_2O:1-xAl_2O_3:1.926SiO_2:xM:128H_2O. We confirmed our LTA synthesis via characterization with XRD (Figure 16).

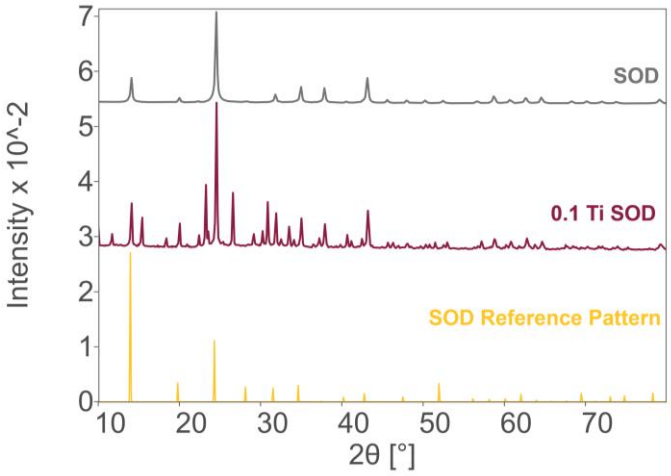

Figure 15. XRD pattern of 0.1 Ti SOD (maroon line) and unsubstituted SOD (gray line) synthesized using the Al-Last method. Calculated SOD reference pattern (yellow line) is provided by IZA.

Besides VPI-5 and ABW, all synthesized zeolite frameworks showed the correct characteristic peaks when we characterized them with XRD. However, when put on the TGA for oxygen adsorption experiments, all synthesized samples failed to show any mass increase during oxygen flow. This led us to start looking toward other classes of adsorbent materials.

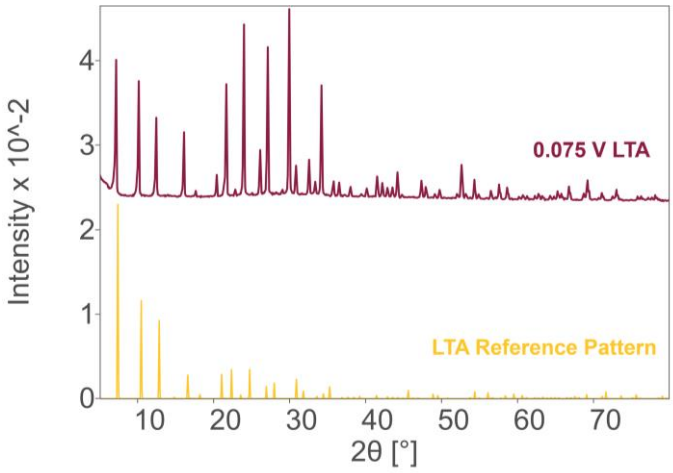

Figure 16. XRD pattern of 0.075 V LTA (maroon line) synthesized using the Al-Last method. Calculated LTA reference pattern (yellow line) is provided by IZA.

3.2. POROUS $YBaCo_4O_{7+\delta}$ (YBC) SYNTHESIS, CHARACTERIZATION, AND OXYGEN SORPTION

After we developed the Al-last synthesis method, we also started investigating different sorbent materials, to mitigate the challenges we were having with heteroatom substitution into

the zeolite framework. We decided to focus on the metal oxide, $YBaCo_4O_{7+\delta}$ (YBC), another oxygen storage material. However, YBC has slow adsorption kinetics and a high oxygen desorption temperature, which limits its application in thermally driven sorption cycles. We hypothesized

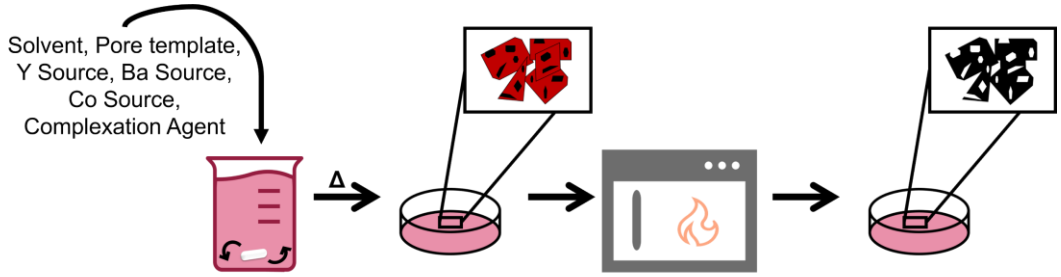

Figure 17. Generalized synthesis method for porous YBC, showing metal precursor mixing, drying to form the gel, then calcination to burn off the pore template and sinter the material.

that the kinetics of YBC could be improved by inducing mesopores (2-50 nm pore diameters) into the material, as more of the material surface is available to the adsorbate, and the need for bulk diffusion is significantly reduced, to ~1-10 nm.

In our first porous YBC synthesis attempt, we modified the method outlined in Yang et al.[11] for mesoporous metal oxide fabrication. We dissolved appropriate stoichiometric amounts of yittrium oxide, cobalt nitrate, and barium carbonate in ethanol, then added Pluronic 123 (P123) as the pore-forming agent (100 g of P123:total mols metal). We then dried the solution at 120°C for 48 hours, then calcined the resulting powder at 1000°C for ten hours in air. Figure 17 shows a generalized method for synthesizing porous YBC.

We characterized YBC porosity and surface area via nitrogen physisorption. We obtained physisorption curves (-196 °C) on a Micrometrics 3Flex to calculate BET surface areas and pore volumes. However, the physisorption curve in Figure 18 lacks a defined hysteresis loop that is indicative of defined mesopores. The sharp increase in the adsorption isotherm close to P/P0 = 1 indicates capillary condensation between particles at high pressure. We derived Brunauer-Emmett-Teller (BET) surface area values and pore volume distributions from the N_2 physisorption curve. The BET surface area of the porous YBC sample, was approximately, 15 times higher than that of the nonporous YBC sample (Table 1), owing to the increase in pore volume. However, this result does not agree with the small hysteresis loop in the physisorption curve, we expect that a mesoporous sample would have a larger loop closer to P/P_0=1. This irregular result led us to develop additional material synthesis methods, to deter-

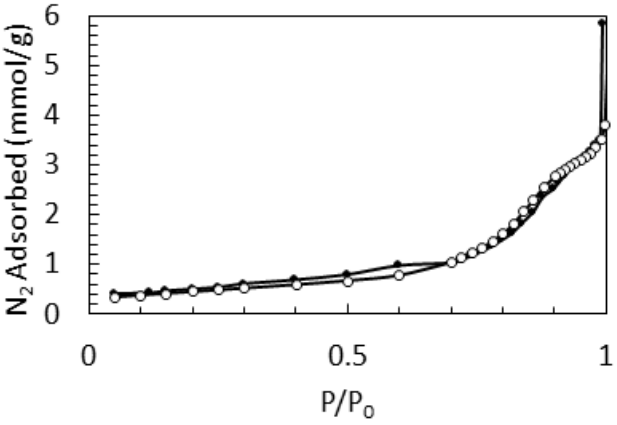

Figure 18. N2 physisorption curve of our first porous YBC synthesis. Black circles indicate N2 adsorption and white circles indicate N2 desorption.

mine the optimal conditions to form the mesopores, and increased surface area.

Table 1. BET surface area and pore volume values derived from N_2 physisorption.

	Pore Treatment	Nonporous YBC
S_{BET} (m^2/g)	37.4	2.42
V_{Pore} (cm^3/g)	0.118	0.018

After our first synthesis attempt, we developed a new porous YBC synthesis method based on previously published work using a modified[12] Pechini sol-gel method. In which, we dissolved appropriate stoichiometric amounts of yttrium oxide, cobalt nitrate, and barium carbonate in nitric acid, along with excess ethylenediaminetetraacetic acid (EDTA) as a chelating agent. We heated the solution to ~200°C on a magnetic stir plate, until the mixture self-burned to fluffy ashes. We then calcined the resulting powder at 1000°C for ten hours in air.

Shortly after this, we developed two additional synthesis methods, based on published YBC syntheses and porous metal oxide synthesis literature; one modified Pechini sol-gel method[13] and one citrate chelating solution method.[14] In the citric acid (CA) method, we dissolved appropriate stoichiometric amounts of yttrium nitrate, cobalt nitrate, and barium nitrate in water, along with excess citric acid as a chelating agent. After stirring for 1 hour, we added the pore template, P123 (100 g of P123:total metal mols), dissolved in 10 mL of ethanol, and stirred the resulting solution for an additional hour. We then dried the solution at 140°C for 48 hours and calcined the resulting powder at 1000°C for 10 hours in air. In the citrate chelating solution (CS) method, we dissolved appropriate stoichiometric amounts of yttrium nitrate, cobalt nitrate, and barium carbonate in ethanol along with excess citric acid (CA) as a chelating agent. We then dried the solution at 45°C for 36 hours in a vacuum oven, until a gel formed. We re-dissolved the gel in water to create a 1 M citrate solution and stirred the solution overnight. The following day, we dissolved a calculated amount of the pore template (100 g of P123:total metal mols), Pluronic F-127, in 10 mL of a 4:1 water:ethanol mixture and then added 4 mL of the citrate solution. We then dried the solution at 100°C for 40 hours and calcined the resulting powder at 1000°C for ten hours in air.

We confirmed the formation of YBC particles by observation of characteristic powder XRD peaks for $YBaCo_4O_{7+\delta}$ at 2ϑ = 28-30°, 2ϑ = 31°, and 2ϑ = 33-35°(Figure 19). All the synthesized samples show an extraneous Y_2O_3 peak at 2ϑ = 29°. After characterization, we found that the EDTA method yielded the most crystalline samples. We then chose to evaluate this sample in oxygen cycling experiments.

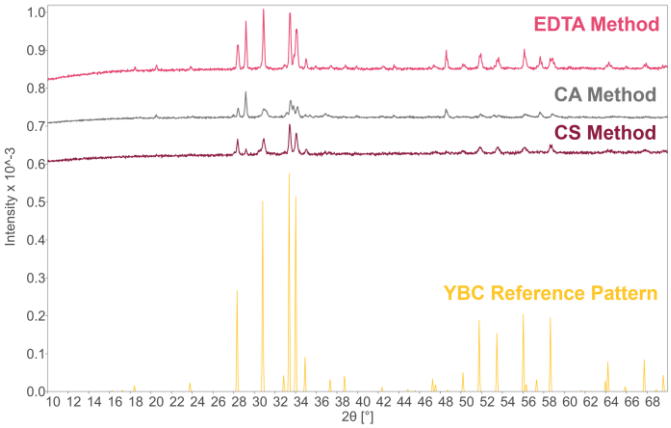

Figure 19. XRD patterns of YBC samples synthesized with the EDTA method (pink line), the CA method (gray line), the CS method (maroon line), and the YBC reference pattern (yellow line, PDF#04-012-7225).

We evaluated the oxygen adsorption capacity of our porous YBC sample synthesized with the EDTA method in a thermogravimetric analyzer (TGA). During the cycling experiment, we preheated approximately 20 mg of the sorbent to 400 °C, then cooled to 275 °C under flowing Ar to prepare the sorbent surface. Then the sample was held at 275 °C in a 20% O_2/Ar mixture for 1 hour and the entire process was repeated (Figure 20). The percent mass change in each cycle was approximately 2.5% throughout the experiment. This 2.5% mass increase corresponds to an oxygen capacity of 0.89 mol O/mol YBC sample. We then used the mass change versus time data to evaluate the oxygen kinetics of the sorbent.

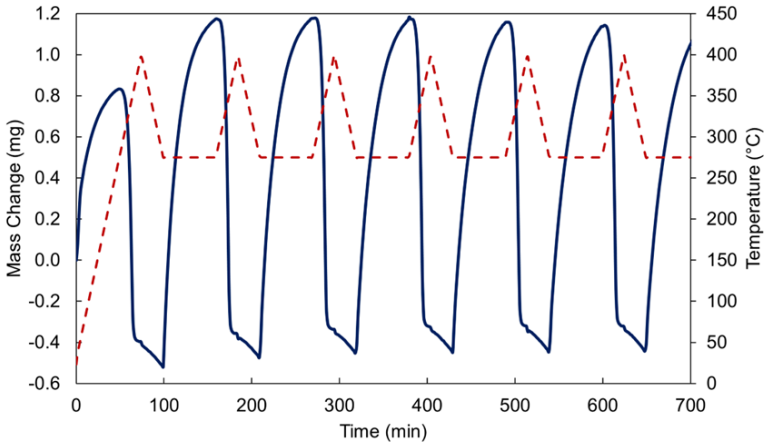

Figure 20. Mass change (blue line) and temperature (red dotted line) versus time of porous YBC at 275° (graph not background corrected).

We represent oxygen nonstoichiometry, the number of oxygen atoms per unit cell of $YBaCo_4O_{7+\delta}$ in excess of seven, with the symbol δ. The relationship between δ and the percent mass change from the TGA experiment is given by:

$$\delta = \frac{Mass\ Change\ \%/Molar\ Mass\ O}{Molar\ Mass\ YBC/100\ \%} \quad (14).$$

We then plot the δ values over time for porous YBC (EDTA method) and nonporous YBC (Figure 21). When we compared porous YBC to its nonporous analog, the porous YBC sample achieved higher δ values at earlier times. To understand oxygen adsorption rate kinetics, we then analyzed δ values with the following pseudo-second-order rate model:

$$\delta = \delta_e^2 kt / (1 + \delta_e) kt \cdot \quad (15).$$

In which, k is the pseudo-second-order rate constant, t is time, and δ_e is adsorption capacity at equilibrium. The values of k for porous YBC and conventional YBC were 0.097 min^{-1} and 0.044 min^{-1}, respectively. These rate constant values indicate that porous YBC has faster oxygen kinetics than its nonporous analog. This supports our hypothesis that the addition of a pore network

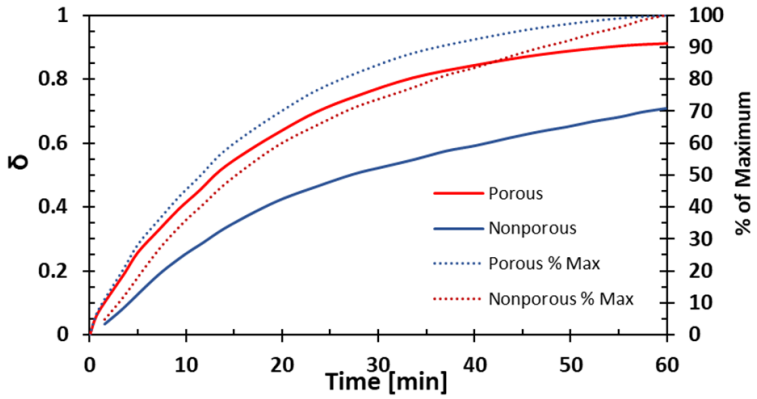

Figure 21. δ values versus time of porous YBC synthesized with the EDTA method (blue line) and conventional YBC (red line).

improves oxygen kinetics. However, we were unable to confirm this hypothesis by characterizing the BET surface area and porosity of our porous YBC samples, due to instrument shutdown. Our future work will aim to further understand the relationship between porosity and oxygen kinetics in YBC sorbents.

The two most important outcomes of the synthesis work are (1) it is feasible to synthesize high surface-area oxygen sorbents, and adsorption/desorption kinetics can be significantly improved by increasing the surface area, and (2) synthesizing targeted substituted zeolites is challenging and methods need to be improved in order to systematically synthesize and characterize them, especially as a tool for validating gas-solid thermodynamic and density functional theory models.

4. COMPUTATIONAL MATERIALS SCREENING

4.1. COMPUTATIONAL METHODS: DENSITY FUNCTIONAL THEORY AND MACHINE LEARNING

Even though computational materials discovery was an aspect of the project that we deemphasized, for completeness we report here the methods and salient results, including relevant results from our prior work.[15] As in Wilson et al., we conducted density functional theory (DFT) calculations using the Vienna Ab Initio Simulation Package (VASP), with periodic boundary conditions, and the Perdew-Burke-Ernzerhof (PBE) generalized gradient approximation (GGA) functional. Projector augmented wave (PAW) pseudopotentials were used to eliminate computational costs associated with calculating non-participating core electrons. Our PAWs explicitly calculated the 3s and 3p orbitals for Al and P, and the 2s and 2p orbitals for O. For most dopants, we considered only valence electrons, with the exception of Ce and Pr, for which we included 4f, 5s, 5p, 5d and 6s orbitals, and Zr for which we included 4s, 4p, 5s, and 4d orbitals. We note that all substitutions result in overall system charge neutrality. Wavefunctions are represented as a summation of plane waves with energies up to 500 eV, chosen because there is only a 1×10^{-8} eV difference in O_2 adsorption energy on Sn doped AlPO5 between planewaves up to 500 eV and 600 eV. We sampled the Brillion zone at the Γ-point. Convergence studies found only a 0.026 eV structural energy difference between a 2x2x2 Monkhorst Pack k-point mesh and Γ-point calculations of neat ALPO-5.

We used HSE06 functional calculations to validate the PBE results. We find that PBE energies are in good agreement with the HSE06 calculations. Thus, we did all the remaining calculations, unless otherwise noted, with the PBE functional, which is significantly less computationally expensive.

We define the binding energy as

$$E_b = E_{ads} - (E_{base} + E_{O_2}) \tag{16}$$

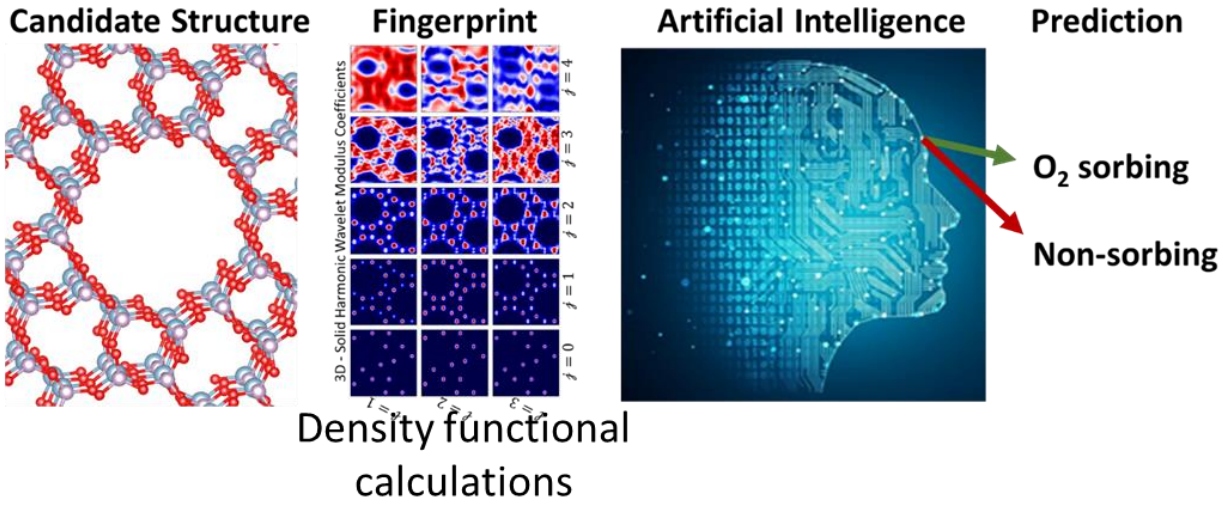

Figure 22. High-level step-by-step illustration of the computational materials screening approach.

where E_b is the adsorption energy for O_2, E_{ads} is the calculated energy of O_2 adsorbed to the surface, E_{base} is the energy of the structure with no molecular oxygen present, and E_{O_2} is the energy of molecular oxygen in vacuum. A negative adsorption energy indicates an exothermic adsorption process.

While density functional theory calculations offer excellent computational accuracy, they are also computationally demanding and not suitable for large-scale materials screening such as the tens of thousands of structures envisioned for this project. To enable such broad screening, we used DFT to "fingerprint" candidate structure properties, to then use as a training set for machine learning (ML) algorithms, which are then able to rapidly screen through many candidate structures and identify those with likely desirable properties, primarily binding energy, but also stability and others. Once identified, this much smaller set of structures can be further and accurately characterized and down-selected via DFT. The process is schematically illustrated in Figure 22.

4.2. RESULTS

The most important result of the computational sorbent screening work is summarized in Figure 23. With the ML classification network, which utilizes a 3D scattered wavelet algorithm, it was predicted that out of 138,478 different substituted zeolite structures, 39,137 structures (28%) are expected to chemisorb O_2, with an energy of at least 0.2 eV. It is noteworthy that majority of the screened zeolites did not show oxygen chemisorption, a fact somewhat reflective of the difficulty of the problem and the lack of "standard" oxygen adsorbing zeolites.

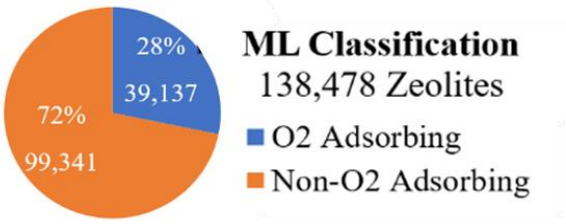

Figure 23. Machine learning zeolite screening results.

Although not strictly necessary for the intended spaceflight application, for experimental purposes we further down-selected from the large number of sorbing substituted zeolites. To down-select the zeolites for synthesis, we first prioritized the cost of the substitutional elements. When only considering substituted zeolites with Fe, Sn, Ce, or Ni, the number of candidate structures dramatically reduces from 39,137 pre-screened material candidates to (a still substantial) 3,393. This new list includes 111 zeolite structure types. We further down-select by only choosing those with the respectively largest average diffusing sphere sizes (4.5 Å and larger). The basis of this decision is to facilitate substitutional atom migration into the zeolite channel during synthesis and allow for efficient O_2 diffusion into the channel during operation. This narrows the list of

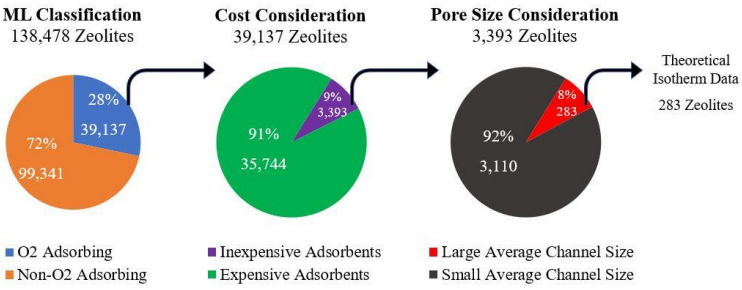

Figure 24. Down-selection for experimental synthesis of oxygen-adsorbing substituted zeolites.

candidates to 283 zeolites, encompassing nine distinct structure types (Beta Polymorph A, ECR-34, EMM-23, Gmelinite, MAPSO-46, Mazzite, PKU-16, STA-1, VPI-5)

Not immediately evident in Figure 23 is a binding energy is calculated for each screened zeolite. To be suitable for oxygen harvesting on Mars, the numerous adsorbing zeolites must also have binding energies in the range determined by the gas-solid thermodynamic models from Chapter 2. An example of binding energies for several substituted ALPO-5 zeolites, of particular interest because of their structure suitable for substitution, is in Figure 25. The shaded region corresponds to the upper end of the binding energy range identified in Chapter 2.

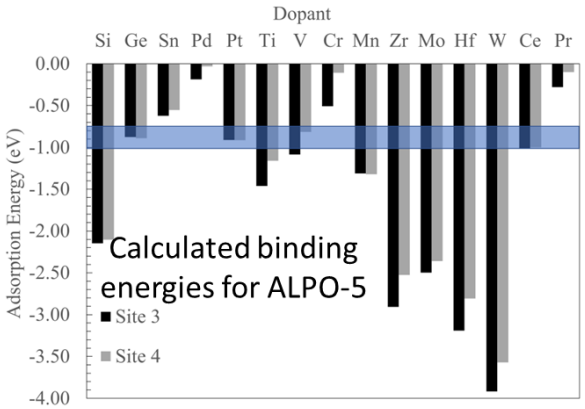

Figure 25. Binding energies for substituted ALPO-5.

Recalling that selectivity is one of the anticipated features of chemisorption, also critical for the intended oxygen harvesting application, we evaluated the binding energy for competing gases from the Mars atmosphere: CO_2, N_2, CO, and H_2. We include hydrogen in anticipation of the need to purify it as part of its generation from locally sourced water.

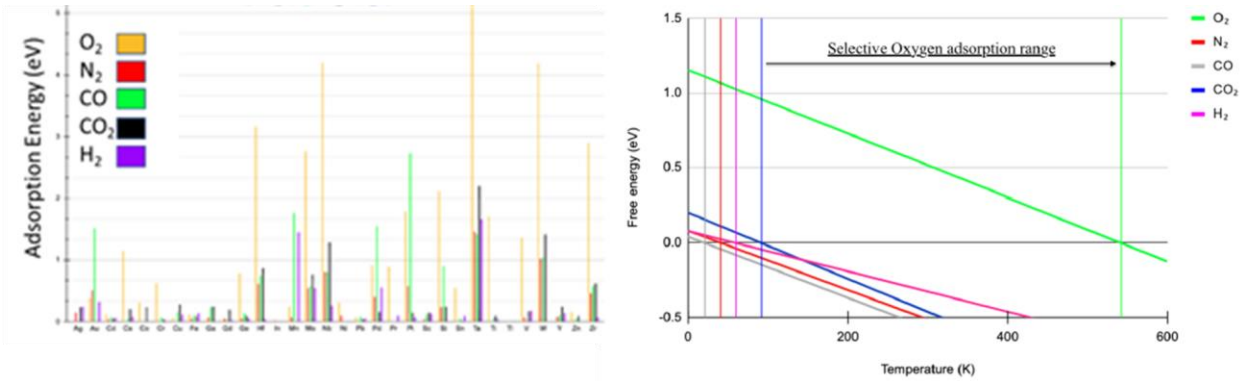

Figure 26. Comparison of binding energies and free energies of adsorption between oxygen on the one hand and. competing gases from the Mars atmosphere: CO_2, N_2, CO, and H_2.

The most important conclusions from these comparison calculations are that for properly selected substituted zeolites the binding energy for competing gases is substantially lower than for oxygen—so lower that the free energy of adsorption is negative for all anticipated operating temperatures. In conclusion, while oxygen binding is predicted to be sufficient (and tunable) for the TSSD oxygen harvesting, the process would reject unwanted gas impurities entirely.

5. OXYGEN HARVESTING DEVICE DESIGN

Processing large volumes of gas to separate a minority component inevitably poses the question of the mechanical work input necessary to move these large gas volumes, which in the case of oxygen on Mars is at a minimum 625 m^3 of ambient air for every m^3 of harvested oxygen, owing to the O_2 concentration of 1600 ppm. Assuming not all oxygen is removed from the mixture, a ratio of ~1000:1 is plausible.

Terrestrial precedent exists for this kind of process, namely CO_2 capture from the Earth atmosphere, typically referred to as direct air capture or DAC, motivated by climate change mitigation. The feasibility of DAC, removing CO_2 from an even lower concentration of ~400 ppm was in part responsible for our confidence that direct O_2 capture on Mars is also feasible. These two processes share the challenge of mechanical work for moving large amounts of ambient air. In the case of DAC, some approaches are entirely passive, relying on natural air motion. The main challenge of naturally ventilated systems is the compromise the approach necessarily makes with device size, necessitating a comparatively large device per unit output.

An additional and significant challenge in the Mars environment with respect to air processing is dust fouling, which in some form or another could necessitate filtering and associated filter maintenance or replacement and additional pressure drop. This issue would be especially prominent in a standard separation type of column, where the sorbent is packed in a tubular bed.

Finally, irrespective of the particular implementation, an important factor in gas-solid interactions is the formation of a stagnant boundary layer through which gas exchange occurs by molecular diffusion, and therefore much more slowly than in turbulent flow areas. Thinning the boundary layer would have the effect of accelerating reaction kinetics and therefore decreasing cycle times and total sorbent needs.

After much consideration and literature review, we opted for a design that, we believe, addresses all the above challenges without introducing significant new ones. The centrifugal TSSD

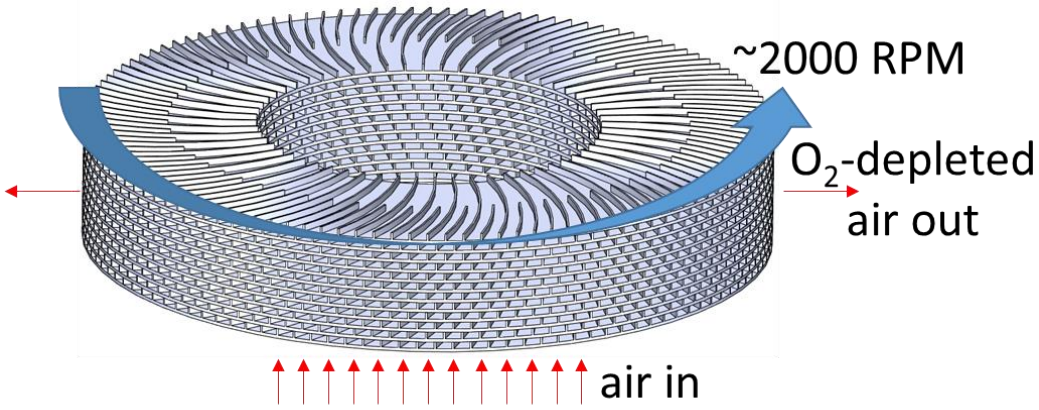

Figure 27. Centrifugal TSSD oxygen separator contactor concept. The envisioned diameter is ~15 cm. The top cover is absent in the image, for clarity.

oxygen separator shown in Figure 27 consists of a stack of finned rotating disks, either constructed of or coated with a high-surface area sorbent.

The envisioned principle of operation is straightforward: The stack of rotating disks ingests air through the central opening and ejects oxygen-depleted through the cylinder sides. As air flows over the finned disks, molecules come in repeated contact with the surface, to maximize the probability of adsorption. Viscous drag drives the airflow in whole or in part.

The centrifugal separator has much in common with an extensively studied concept in heat management, the Sandia Cooler. In this report, we focus on the aspects relevant to TSSD oxygen separation on Mars and refer the reader to the extensive reporting on the Sandia Cooler for further details.[16,17]

The centrifugal TSSD separator derives its key performance potential from a subtle but critical distinction, compared to stationary air contactor designs. Instead of relying solely on forced air moving over a contactor structure (including packed beds), the contactor itself rotates at ~2000 RPM, combining a contactor with a centrifugal blower. The key physical difference of a contactor in a rotating (non-inertial) reference frame are rotation-generated inertial forces, which significantly thin the stagnant boundary layer of air next to the surface, enhancing gas-solid interaction and violently ejecting dust particles.

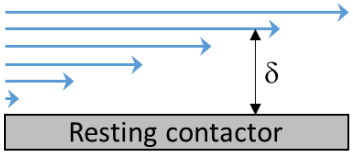

Figure 28. Air in the boundary layer next to a stationary contactor surface accelerates by viscous drag with air farther away. δ is the boundary layer thickness.

Qualitatively, the boundary layer acts as an adherent air blanket (Figure 28), presenting a comparatively thick diffusion region between the gas phase and solid surface, slowing sorption kinetics and facilitating dust accumulation. In a non-inertial reference frame (Figure 29) inertial forces act on *all* air layers equally, accelerating them away from the receiver surface. In the accelerated case the boundary layer can be significantly thinned relative to the stationary case, thus vastly increasing the convection coefficient, which increases the gas particle flux exchange. The relatively thin boundary layer also brings high speed air close to the surface of the receiver, facilitating self-cleaning and inhibiting the accumulation of dust and other fouling.

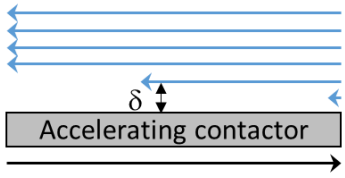

Figure 29. With a moving and accelerating contactor, inertial forces accelerate all air layers equally, shearing and substantially thinning the boundary layer (δ).

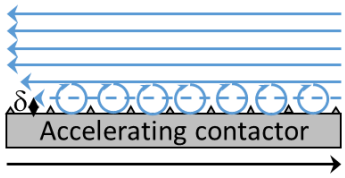

Figure 30. Surface morphology disrupts the laminar boundary layer, introducing turbulent heat mixing.

Adjusting the macro- and meso-scale surface morphology amplifies the benefits of the rotating contactor, by intentionally introducing turbulence in the (laminar) boundary layer, causing its frequent disruption and re-forming. Turbulence further thins the boundary layer and promotes mixing, additionally increasing the convection coefficient.

The geometry also provides pumping analogous to a centrifugal compressor, reducing, and possibly eliminating the need for additional air moving equipment.

The most direct, thorough, and validated investigation of the key elements of the centrifugal TSSD separator has been for CPU cooling. Near-ambient temperature studies have shown that small diameter units (D~0.1 m) achieve most of the heat transfer benefits, notably a convection coefficient boost from ~100 W/m^{2}K to over 2500 W/m^{2}K at a rotation rate of ~3000 RPM (50 Hz). Our expectation is that the effects of air moving, boundary layer thinning, and dust mitigation will translate well from the Sandia Cooler to the centrifugal separator.

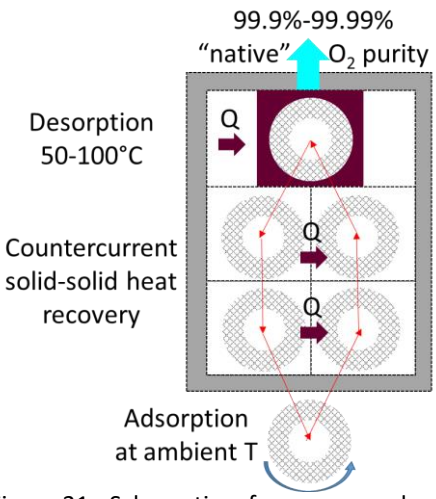

Figure 31. Schematic of an oxygen harvesting system consisting of six contactors. For simplicity, operable interior and exterior openings are not shown.

The design being at the conceptual stage, the main objective of the preliminary performance models we constructed was to broadly determine the mass of the reactive components, which likely to be the main driver of the overall mass of the separation system. We base our mass estimate on a harvesting system with six contactors, moving between the ambient and several interior chambers, illustrated in Figure 31. As shown in the figure, the main steps of the separation process are: Adsorption at T_{amb}, the only step during which high-speed rotation is necessary; Contercurrent solid-solid heat recovery, here shown in two stages; and Desorption using external heat input.

For a harvesting system using a substituted ALPO-5 sorbent ($1/\lambda$=60, as in the models in Chapter 2), a cycle time of 30 min, and a nominal harvesting rate of 1 kg/day (i.e. sufficient for one person), and a 100% capacity factor (i.e. continuous operation) we arrive to a sorbent mass of ~0.8 kg.

Being mindful of the efficiency penalty of converting heat to work, the above calculation includes a minimized pressure drop in the contactor (~1-5 Pa), which requires relatively low velocity air flows and does somewhat increase the contactor size compared to higher velocities and pressure drops. As a reminder, we initially budgeted a 25 Pa pressure drop, but have, in light of the opportunity afforded by the centrifugal separator concept, revised that to significantly lower values to minimize mechanical work.

6. THE MARS AIR REFINERY

At the conceptual level, and in line with the Reference Architecture, we proposed and began this project under the assumption that the primary energy source for all energy needs on Mars would be nuclear, likely a radioisotope thermoelectric generator (RTG). However, one of the most interesting and potentially far-reaching results of our gas-solid thermodynamic modeling is that energy could also come from an in-situ resource—the Mars atmosphere. If possible, such an approach would considerably decrease the necessary landed mass.

We recall the results shown in Figure 7, indicating that at average ambient temperatures (T_{amb}~217 K) and oxygen delivery at near-ambient pressure (1 kPa), the separation heat input is $Q_{min,O2}$ ~110 kJ/mol. We also recall that the CO concentration in the Mars atmosphere is ~0.07%, a result of the same photolytic process that creates free molecular oxygen (Eq. 1). Taking into account the logarithmic dependence of separation work on concentration (i.e. partial pressure) shown in Eq. 2, and assuming as an approximation that correspondingly higher heat input would be required for CO harvesting than for O_2 harvesting, we arrive to the value of $Q_{min,CO}$~150 kJ/mol.

The above is a very interesting result. Adding Q_{min} for a mole of oxygen and two moles of CO we arrive to a value $Q_{min,tot}$~410 kJ/mol. This value is considerably lower than the enthalpy of CO oxidation per the formula:

$$O_2 + 2CO \rightarrow 2CO_2 + 572\ kJ/mol_{O2} \quad (17).$$

Put differently, if oxygen and CO harvesting can be as efficient as gas-solid models predict, part of the harvested products can be re-oxidized exothermically to sustain the process indefinitely without further external energy input. The remaining “free” oxygen and CO (~25% of the originally harvested quantity) can be set aside for life support and propellant needs, as well as for power generation via solid-oxide fuel cells. Any remaining CO can also be used to react with locally sourced water to produce hydrogen via the classic (exothermic) water-gas shift reaction (WGSR):

$$CO + H_2O \rightleftharpoons CO_2 + H_2 \quad (18).$$

We term the overall process ‘Mars Air Refinery’ (Figure 32), as it would operate in analogy to refineries on Earth. The distinction between the two is that the oxygen and CO resources on Mars are entirely renewable via the solar photolysis process of Eq. 1.

If feasible, the Mars Air Refinery could be a radical game-changer in terms of mission planning, specifically with respect to the power plant that would need to be landed on Mars. Instead of a ‘full size’ power plant, a much smaller (‘ignition’) one would be required, to start the process, which could then ramp up and self-sustainably operate at a full capacity power level much exceeding the original ‘ignition’ power source. Notably, the comparatively small ‘ignition’ source need not be nuclear, but can likely be photovoltaic.

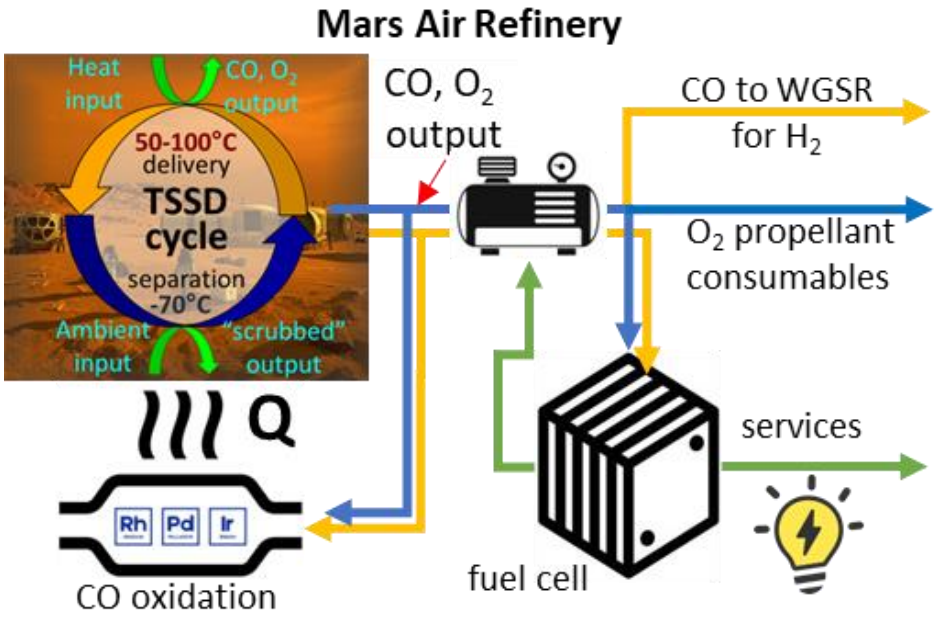

Figure 32. Schematic process diagram of the Mars Air Refinery.

It bears emphasizing that the key enabling aspect of TSSD oxygen harvesting and the Mars Air refinery is the reliance on heat input and minimization of mechanical work. For example, in the schematic diagram in Figure 32, the TSSD input is heat, and the output is at or slightly above ambient pressure, almost entirely free of mechanical work input. (The primary mechanical work input is for centrifugal separator rotation.)

To further minimize mechanical work, in the schematic above, for example, the pressure in the fuel cell could also be minimized to the value necessary for operation in a reasonably-sized unit. Likewise, CO flowing to the WGSR for hydrogen production could also be minimized, reserving mechanical compression work only for the services for which it is necessary.

So far we have taken great care to minimize conversion to electricity and mechanical work. This focus has been primarily driven by the poor heat-to-electricity conversion of RTG units of ~6%. The Mars Air Refinery would offer significant improvements in this respect. As shown in Figure 32, in the 'energy independence on Mars' scenario, the power plant is a solid oxide fuel cell, a device with a much higher conversion efficiency (~50%) than an RTG. Notably, SOFCs also co-generate heat at ~800°C. This is to say that, if feasible, the Mars Air Refinery would also significantly change for the better the value ratio between heat and electricity/mechanical work and widen the operating parameter space for electro-mechanical applications.

Finally, to illustrate the potential of the Mars Air Refinery, let us consider a simplified example refinery sized to harvest 1000 kg of oxygen per day (24 h). This rate would correspond to 31250 mol/day or 0.36 mol/s. The stoichiometrically corresponding CO harvesting rate is 1750 kg/day (0.72 mol/s). Re-using 75% of the products to sustain the harvesting process leaves 25% for combined heat and power generation. These remaining 25%, recombined in a fuel cell with 50% efficiency would generate ~25 kW_e of electric power and an equal amount of high-

quality heat.

We also consider the mass implications, comparing an RTG with a refinery + fuel cell combination. A general purpose 300 W RTG has a power-to-mass ratio of about 5 W_e/kg. A 25 kW_e unit would then have mass of ~5,000 kg, though with potential savings at scale. In contrast, a Mars Air Refinery of the same output, based on the above estimates for oxygen harvesting would have a mass of ~2,500 kg.

In summary, there appears to be a significant opportunity to at least diversify, and potentially even replace nuclear power sources on Mars with ISRU chemical resources, warranting a considerably more detailed study, especially with respect to sorbent synthesis and model validation, and detailed device design and component testing under representative conditions.

7. EDUCATION AND OUTREACH

Two graduate students were supported by this project:

- Natalia Ali, PhD student in chemical engineering at ASU
- Zoe Liberman-Martin, MS student in chemical engineering at ASU

Though short in duration, the project also attracted significant interest by undergraduate students from the ASU School of Sustainability, School for the Future of Innovations in Society, and the Fulton Schools of Engineering (chemical engineering), who were able to contribute to it via background research and chemical synthesis in the laboratory: Nicolas Garnand, Jingzhi Xue, Jared Bridges, Ian Padgett, and Iris Calderon.

The Mars oxygen harvesting and closely related topics have been presented by Ivan Ermanoski in two presentation before diverse audiences.

The 2022 NIAC symposium in Tucson, AZ, September 20-22, 2022

The XXIII Space Resources Roundtable, Colorado School of Mines, Golden, CO, June 6-9/2023

8. FUTURE STUDIES

Recommendations for advancing the technologies for oxygen harvesting are provided below. These recommendations are primarily guided by the outcomes of the present study, though also taking into account lessons learned from MOXIE and MARRS.

1. EXPERIMENTALLY SYNTHESIZE AND CHARACTERIZE A HANDFUL OF SUBSTITUTED ZEOLITE OR SIMILAR OXYGEN SORBENTS. This recommendation stems from the need to conclusively show that the material class is a candidate for the TSSD process AND to improve the fidelity of the gas-solid thermodynamic models, which at this time show exceptional promise.
2. EXPERIMENTALLY EVALUATE THE PERFORMANCE PARAMETER SPACE OF THE CENTRIFUGAL SEPARATOR. Given the significant potential to circumvent the challenging issue of air moving and filtration, this recommendation stems from the need to thoroughly understand likely performance in the dust-laden Mars atmosphere.
3. INVESTIGATE THE VALUE OF MULTI-STAGE OXYGEN HARVESTING
4. DETERMINE THE IMPACT OF TSSD ON THE MARS REFERENCE MISSION. This recommendation goes well beyond the conceptual separator design, understanding the need to compare flight-worthy devices on an equal footing.

5. EXPERIMENTALLY SYNTHESIZE AND CHARACTERIZE A HANDFUL OF SUBSTITUTED ZEOLITE OR SIMILAR CARBON MONOXIDE SORBENTS. This recommendation stems from the game-changing potential to almost entirely supplant the need for including a nuclear power plant in human Mars missions.
6. INVESTIGATE THE VALUE OF OXYGEN, CARBON MONOXIDE, AND NITROGEN CO-HARVESTING. In analogy to standard refineries and more broadly separation processes, there could be substantial advantages in co-harvesting useful gases, especially with respect to minimizing the mechanical work per unit product.

REFERENCES

[1] "Human Exploration of Mars Design Reference Architecture 5.0" NASA, 2009; "Human Exploration of Mars Design Reference Architecture 5.0 Addendum" NASA 2013

[2] Jeffrey A. Hoffman et al., Mars Oxygen ISRU Experiment (MOXIE)—Preparing for human Mars exploration, Sci. Adv. 8, eabp8636(2022). DOI: 10.1126/sciadv.abp8636

[3] Mars Fact Sheet, NASA, https://nssdc.gsfc.nasa.gov/planetary/factsheet/marsfact.html

[4] Mars Atmosphere Resource Recovery System, (MARRS), Final Report NIAC/USRA Phase I Research Grant # 07600-046

[5] Hecht, M. H., and Hoffman, J. A., 2016 "The Mars Oxygen ISRU Experiment (MOXIE) on the Mars 2020 Rover"

[6] "Thermally-driven adsorption/desorption cycle for oxygen pumping in thermochemical fuel production", I. Ermanoski, E. B. Stechel, Solar Energy 198 (2020) 578 https://doi.org/10.1016/j.solener.2020.01.050

[7] "Substituted ALPO-5 Zeolites as Promising O_2 Sorption Pump Materials: A Density Functional Theory Study", S. Wilson, E. B. Stechel, I. Ermanoski, C. Muhich, J. Phys. Chem. C, 125 (2021), 1269–1281

[8] Olson, G.B., Kuehmann, C.J., 2014. Materials genomics: From CALPHAD to flight. Scripta Materialia 70, 25–30. https://doi.org/10.1016/j.scriptamat.2013.08.032

[9] Hentit, H.; Bachari, K.; Ouali, M. S.; Womes, M.; Benaichouba, B.; Jumas, J. C. Alkylation of Benzene and Other Aromatics by Benzyl Chloride over Iron-Containing Aluminophosphate Molecular Sieves. J. Mol. Catal. A Chem. 2007, 275 (1–2), 158–166. https://doi.org/10.1016/j.molcata.2007.05.032.

Cardile, C. M.; Tapp, N. J.; Milestone, N. B. Synthesis and Characterization of an Iron-Substituted Aluminophosphate Molecular Sieve. Zeolites 1990, 10 (2), 90–94. https://doi.org/10.1016/0144-2449(90)90024-L.

[10] Verified Syntheses of Zeolitic Materials; Robson, Harry, Lillerud, Petter Karl, Ed.; Elsevier, 2001. https://doi.org/10.1016/B978-0-444-50703-7.X5094-7.

[11] Yang, P.; Zhao, D.; Margolese, D. I.; Chmelka, B. F.; Stucky, G. D. Generalized Syntheses of Large-Pore Mesoporous Metal Oxides with Semicrystalline Frameworks. Nat. 1998 3966707 1998, 396 (6707), 152–155. https://doi.org/10.1038/24132.

[12] Xu, M.; Ermanoski, I.; Stechel, E. B.; Deng, S. Oxygen Pumping Characteristics of YBaCo4O7+δ for Solar Thermochemical Cycles. Chem. Eng. J. 2020, 389 (October 2019), 124026. https://doi.org/10.1016/j.cej.2020.124026.

[13] Karen, P.; Kjekshus, A. Citrate-Gel Syntheses in the Y(O)–Ba(O)–Cu(O) System. J. Am. Ceram. Soc. 1994, 77 (2), 547–552. https://doi.org/10.1111/J.1151-2916.1994.TB07028.X.

[14] Wang, C.; Wan, X.; Duan, L.; Zeng, P.; Liu, L.; Guo, D.; Xia, Y.; Elzatahry, A. A.; Xia, Y.; Li, W.; Zhao, D. Molecular Design Strategy for Ordered Mesoporous Stoichiometric Metal Oxide. Angew. Chemie Int. Ed. 2019, 58 (44), 15863–15868. https://doi.org/10.1002/anie.201907748.

[15] "Substituted ALPO-5 Zeolites as Promising O_2 Sorption Pump Materials: A Density Functional Theory Study", S. Wilson, E. B. Stechel, I. Ermanoski, C. Muhich, The Journal of Physical Chemistry C, 125 (2021), 1269–1281 https://doi.org/10.1021/acs.jpcc.0c11220

[16] Jeffrey P. Koplow, A Fundamentally New Approach to Air-cooled Heat Exchangers, SANDIA REPORT SAND2010-0258, 2010

[17] Terry A. Johnson et al., Development of the Sandia Cooler, SANDIA REPORT SAND2013-10712, December 2013